Development 140, 2061-2074 (2013) doi:10.1242/dev.062984

An intracellular partitioning-based framework for tissue cell polarity in plants and animals

Katie Abley[1,*], Pierre Barbier de Reuille[1,2,3,*], David Strutt[4], Andrew Bangham[2], Przemyslaw Prusinkiewicz[3], Athanasius F. M. Marée[1], Verônica A. Grieneisen[1,†,‡] and Enrico Coen[1,‡]

Summary

Tissue cell polarity plays a major role in plant and animal development. We propose that a fundamental building block for tissue cell polarity is the process of intracellular partitioning, which can establish individual cell polarity in the absence of asymmetric cues. Coordination of polarities may then arise through cell-cell coupling, which can operate directly, through membrane-spanning complexes, or indirectly, through diffusible molecules. Polarity is anchored to tissues through organisers located at boundaries. We show how this intracellular partitioning-based framework can be applied to both plant and animal systems, allowing different processes to be placed in a common evolutionary and mechanistic context.

Key words: PCP, PIN, Auxin, Organiser, Polarity

Introduction

Many plant and animal tissues exhibit coordinated cell polarities over extended domains. For example, the hairs on a *Drosophila* wing or the distribution of auxin transporters in a developing leaf show highly coordinated orientations (Fig. 1A,B). To understand the mechanisms underlying tissue cell polarity, it helps to define two basic types of coordination: lateral and longitudinal. These types of coordination can be illustrated for a single file of cells, in which polarities are aligned head to tail (longitudinal coordination, Fig. 1C) or aligned lateral to the direction of polarity (lateral coordination, Fig. 1D). Both types of coordination can occur together within a sheet of cells, as the polarity of each cell in the plane may be aligned with both its flanking cells (lateral coordination) and with those ahead or behind it (longitudinal coordination) (Fig. 1E). Similar considerations apply to a three-dimensional (3D) block of cells, except that lateral coordination can be extended to a further dimension (Fig. 1F). A key problem is understanding how such patterns of lateral and longitudinal coordination may be established over extended domains.

One type of model assumes that neighbouring cells have the ability to compare concentrations of specific molecules and align their polarities accordingly. For example, a model for planar polarity coordination in *Drosophila* proposes that the level of Frizzled protein activity in neighbouring cells is compared so that the polarity of each cell becomes oriented towards the neighbour with the lowest Frizzled activity (Simon, 2004; Lawrence et al., 2007). Similarly, it has been proposed that plant cells orient their polarity according to the concentration of auxin in neighbours (Bayer et al., 2009; Jönsson et al., 2006; Smith et al., 2006). Another type of model proposes that polarities are established through differential molecular interactions at cell interfaces, which may be modulated by graded signals. For example, it has been proposed that planar polarity in *Drosophila* depends on establishing different molecular complexes on either side of cell-cell interfaces, with a bias provided by signals that vary across and/or between cells (Amonlirdviman et al., 2005; Le Garrec et al., 2006; Burak and Shraiman, 2009). Yet other types of model propose that polarity depends on measuring molecular fluxes across membranes, concentration gradients across extracellular spaces or gradients in stresses across cells (Mitchison, 1980; Sachs, 1981; Rolland-Lagan and Prusinkiewicz, 2005; Bayer et al., 2009; Heisler et al., 2010; Wabnik et al., 2010). In all of the above models, polarisation of individual cells depends on asymmetric cues or polarisable neighbours.

By contrast, we propose a framework that is based on cells having the ability to polarise in the absence of asymmetric cues or polarisable neighbours, a possibility also suggested by Meinhardt (Meinhardt, 2007). We call this process intracellular partitioning. Tissue cell polarity emerges by coordination of polarities established by intracellular partitioning, through coupling between neighbouring cells (cell-cell coupling) and operation of tissue polarity organisers. To illustrate how the intracellular partitioning-based framework may generate tissue cell polarity patterns, we present a series of simplified theoretical cases and explore their consequences through computer simulations, which are run until a stable state is reached (details of how computer simulations are implemented and the range of parameters explored can be found in supplementary material Appendix S1). For simplicity, we restrict our analysis of tissue cell polarity to one-dimensional (1D) cell files or two-dimensional (2D) cell sheets. The utility of the framework is then illustrated by applying it to canonical examples of tissue cell polarity in plants and animals.

Key features of this framework are as follows. (1) It is applicable to both plant and animal tissue cell polarity. Previous models of tissue cell polarity have considered plant and animal systems separately. We show how both systems may be viewed as involving cell-cell coupling, which may be direct (animals) or indirect (plants). (2) It leads to a new model for polarity coordination in plants. In contrast to previously proposed plant models, the model we propose does not invoke measurement of fluxes, comparison of concentrations between cells, response to physical stresses or measurement of gradients across the thickness of cell walls. (3) It allows different cell polarity systems to be placed in an evolutionary context.

Intracellular partitioning

To illustrate how intracellular partitioning may operate, we consider a simple system with two types of molecular component, A and B, the active forms of which will eventually define opposite

[1]John Innes Centre, Norwich Research Park, Norwich NR4 7UH, UK. [2]School of Computing Sciences, University of East Anglia, Norwich Research Park, Norwich NR4 7TJ, UK. [3]Department of Computer Science, University of Calgary, Calgary, Alberta T2N 1N4, Canada. [4]MRC Centre for Developmental and Biomedical Genetics and Department of Biomedical Science, University of Sheffield, Sheffield S10 2TN, UK.

*These authors contributed equally to this work
‡Authors for correspondence (enrico.coen@jic.ac.uk; veronica.grieneisen@jic.ac.uk)

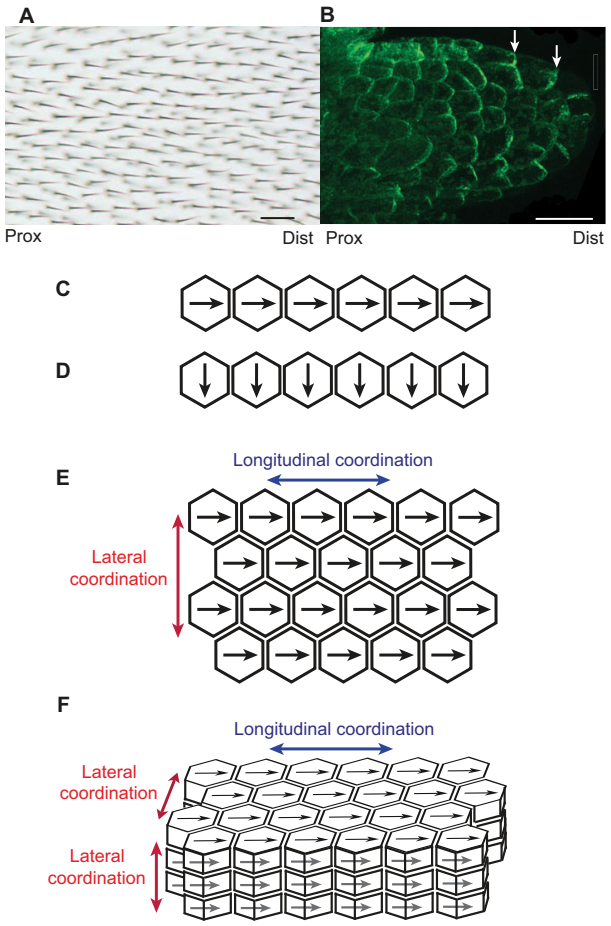

Fig. 1. Polarity coordination. (**A**) Hairs on a *Drosophila* wing point from proximal (Prox) to distal (Dist) positions in a coordinated manner. (**B**) In a developing leaf primordium, the auxin efflux carrier PINFORMED1 [PIN1, visualised using a pPIN1::PIN1:GFP reporter (Benková et al., 2003)] is localised towards the distal end of each cell (arrows). (**C**) Longitudinal coordination occurs in a single file of cells with polarities (indicated by arrows) aligned head to tail. (**D**) Lateral coordination occurs in a single file of cells with polarities aligned lateral to the direction of polarity. (**E**) Longitudinal and lateral coordination can both occur together in a sheet of cells. (**F**) For a 3D block of cells, lateral coordination of polarity may be extended to a further dimension. Scale bars: 20 μm.

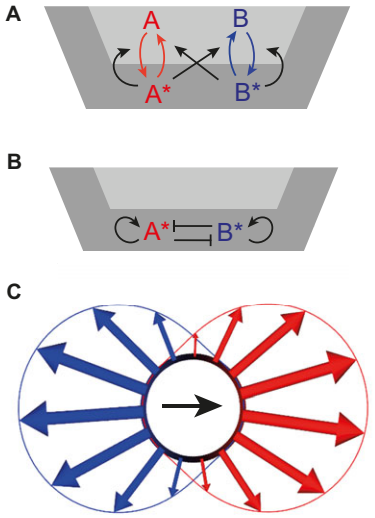

Fig. 2. System for intracellular partitioning. (**A**) Interactions between rapidly diffusing, cytosolic (A,B) and slowly diffusing [membrane-bound (A*,B*)] forms of polarity components (dark-grey compartment represents the membrane). Each polarity component can inter-convert between the inactive form in the cytoplasm and the active membrane-bound form. The active membrane-bound forms of the polarity components (A*,B*) promote membrane binding and activation of their own component, and promote the unbinding and inactivation of the opposite polarity component. (**B**) Short-hand notation for the interactions between polarity components, in which an arrow indicates auto-activation, while a truncated line indicates inhibition by the opposite polarity component. (**C**) Intracellular partitioning resulting from the above interactions. The cell outline is indicated with a black circle. The concentration of A* in the cell membrane is indicated by the distance from the cell outline to the red line (large red arrows indicate a high concentration of A*), whereas the concentration of B* is indicated by the distance to the blue line (large blue arrows indicate a high concentration of B*). Cell polarity in this figure and in all subsequent figures is indicated by the black arrow in the cell that points from high B* to high A*. See supplementary material Appendix S1 for simulation details and parameters.

ends of the cell. In reality, each component may comprise multiple molecular entities; for the sake of simplicity, here we treat each component as a single entity. The components can be in two states: an inactive cytosolic form, A or B, or an active membrane-bound form, A* or B* (Fig. 2A,B). The inactive forms diffuse more rapidly than the active membrane-bound forms. The active forms are autocatalytic (i.e. A* promotes the activation of A to generate more A*) and cross-inhibitory (i.e. A* promotes deactivation of B*, and vice versa). We refer to A, A*, B and B* as polarity components.

Starting from a uniform concentration of polarity components in a cell and small random fluctuations (noise) in the concentrations of A* and B* in the membrane, such a system may lead to a polarised distribution, with a high concentration of A* at one end and B* at the other end of the cell (Fig. 2C). This system is similar to other reaction-diffusion systems that generate polarity within individual cells (Meinhardt, 2007). With an initially uniform distribution of A* and B* across a tissue, and noise within cells (Fig. 3A), intracellular partitioning leads to polarities that are oriented randomly from one cell to the next (Fig. 3B,C; polarity is shown as pointing from the B* to A* cell ends in this figure and in all subsequent figures). Non-polarised cells arise if intracellular partitioning components are absent or fail to interact effectively.

Cell-cell coupling

We build on the notion of intracellular partitioning to generate a more coordinated polarity pattern by incorporating interactions at interfaces of neighbouring cells. This process of cell-cell coupling may lead to local alignment of polarities. Cell-cell coupling may involve direct molecular contacts between juxtaposed cells or indirect interactions mediated by diffusible molecules.

Direct cell-cell coupling

Assume that A* in a given cell can physically interact with B* in the juxtaposed membrane of its neighbour, forming an intercellular A*-B* bridging complex. We can modify the intracellular partitioning mechanism described above such that auto-activation and/or cross-inhibition are influenced by the A*-B* complex; for example, suppose the A*-B* complex inhibits A* on the B* side of the complex (Fig. 4A). Computer simulations of this system

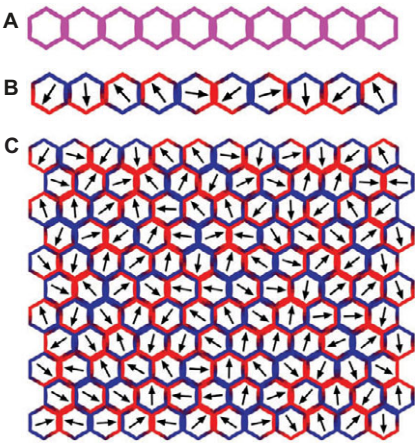

Fig. 3. Polarity pattern through intracellular partitioning. (**A**) A single file of cells in the initial state with A* and B* having a uniform distribution. (**B**) A single file of cells in the final computed state, with polarities resulting from the intracellular partitioning mechanism with no interaction between cells. (**C**) The result of intracellular partitioning with no interactions between cells for a 2D array of cells.

show that an initially uniform (but noisy) distribution of A* and B* in a single file of cells (Fig. 4C) can eventually give rise to regions of aligned polarity (Fig. 4D).

We can extend the role of the A*-B* complex such that all of the auto-activation and cross-inhibition interactions are dependent on it (Fig. 4B). In this case, uncomplexed A* and B* have no role other than allowing formation of A*-B* complexes, while the diffusible A and B forms still play a role in intracellular partitioning. This system also gives rise to regions of locally aligned polarity (Fig. 4E). With this model, an isolated cell (i.e. a cell with no neighbours) no longer becomes polarised because it is unable to form A*-B*complexes. Nevertheless, an individual cell within a group of cells that are incapable of polarising can become polarised through its own intracellular partitioning system (Fig. 4F,G). We use the latter model for all further simulations involving direct cell-cell coupling. A further step towards dependency on neighbours is illustrated by a model for tissue polarity proposed for *Drosophila* in which a diffusible component (C*) creates an effective repulsion between the two orientations of the membrane-spanning complexes (A*-B* and B*-A*) (Burak and Shraiman, 2009). In this model, the B* end of the complex promotes production of C* within the same cell, which then inhibits the complexes in which A* is located within that cell. Considering a cell in isolation this would lead to all complexes being oriented with B* pointing into that cell, because inward-pointing B* can inhibit inward-pointing A* but not vice versa. In the presence of neighbouring cells, inhibition becomes mutual because inward-pointing A* can now inhibit inward-pointing B* by influencing the production of C* in the neighbouring cell (via the B* end of the complex, which points into the neighbour). Consequently, in such a model, polarisation of a cell depends on its neighbours also having an intact polarisation system. All above models can give rise to direct cell-cell coupling but can be distinguished experimentally by defining the cellular contexts under which individual cells can become polarised.

When applied to a 2D array of cells, direct cell-cell coupling models lead to locally coordinated groups of cells or swirled patterns of orientations (e.g. Fig. 4H) (Burak and Shraiman, 2009). In these cases, coordination is both longitudinal and lateral.

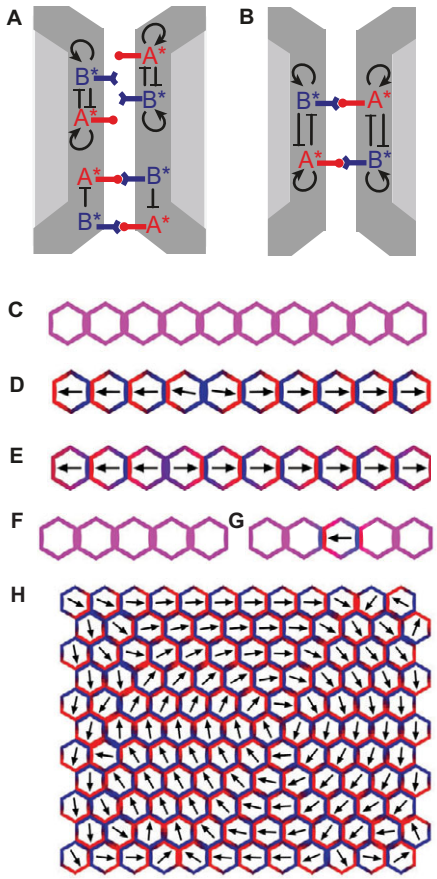

Fig. 4. Direct cell-cell coupling. (**A**) A model for the direct cell-cell coupling system. A* and B* in the membrane of each cell (dark-grey compartment) may interact across the intercellular space to form an A*-B* bridging complex. The complex inhibits A* on the B* side of the complex. Interactions between uncomplexed A* and B* components lead to intracellular partitioning. (**B**) Model in which all of the auto-activation and cross-inhibition interactions are dependent on formation of the A*-B* bridging complex. (**C**) Initial state of direct cell-cell coupling system for a single file of cells. (**D**) Result of direct cell-cell coupling using the interactions described in A for a single file of cells. Two groups with coordinated polarity have formed (a group of four cells with polarity pointing left and a group of six cells with polarity pointing right). (**E**) Result of direct cell-cell coupling using the interactions described in B for a single file of cells. (**F**) Cells do not become polarised when the A and B components have the same diffusion constants as A* and B*. (**G**) Restoration of the higher diffusion rate for A and B to the central cell leads to it becoming polarised, even though its neighbours retain the lower diffusion rate for A and B, and thus do not have the ability to polarise. (**H**) Direct cell-cell coupling in a 2D array of cells. Polarities show swirled organisation with local stretches of coordination.

Indirect cell-cell coupling

Consider again the direct cell-cell coupling model in which the only role of the A*-B* membrane-spanning complex is inhibition of A* at the B* end of the complex (Fig. 4A). With this system, A* in one cell effectively inhibits formation of A* in the juxtaposed membrane of its neighbour. In Fig. 5A, we show a parsimonious way of achieving an equivalent process without direct cell-cell contacts. In this case, A* in one cell promotes export of a small mediator molecule, M (green dot), which can diffuse through the extracellular space. This extracellular M triggers a membrane receptor that then locally inhibits A* in the membrane (i.e. M

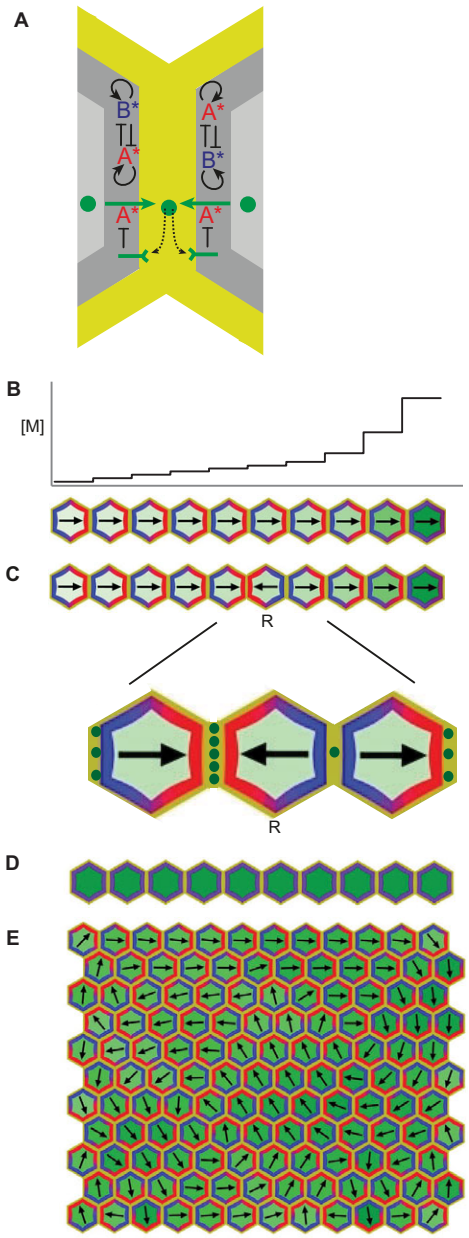

Fig. 5. Indirect cell-cell coupling. (**A**) Interactions at a cell-cell interface for an indirect cell-cell coupling mechanism in which A* in the membrane (dark-grey compartment) promotes export (green arrow) of a small mediating molecule, M (green circles), that can diffuse through the cell wall (yellow compartment) and trigger a receptor (green Y-shape) that then inhibits A*. The distributions of A* and B* become polarised through intracellular partitioning. (**B**) Indirect cell-cell coupling for a single file of cells. The graph shows the total intracellular concentration of M in each cell in the file. The concentration of intracellular M in each cell is also indicated by the intensity of green in the file of cells (bottom). For cell walls at the outer boundary of the tissue, there is no exchange of M with the surrounding medium. (**C**) The cell labelled R has an opposite polarity with respect to the rest of the cells in the file. In the left wall of cell R, high levels of M (green circles) accumulate and inhibit A* in both adjacent membranes. In the right wall of cell R, low levels of M favour A*. The net result of these interactions is that the polarity of the R cell reverses and thus aligns with the rest of the file. (**D**) If polarity components do not auto-activate and mutually inhibit there is no intracellular partitioning and polarity is lost with an indirect cell-cell coupling system. (**E**) Result of indirect cell-cell coupling for a 2D array of cells. Polarities show swirled organisation with local stretches of coordination.

favours B* over A*). This system could allow A* in the cell exporting M to inhibit A* in its neighbour. However, an apparent problem is that extracellular M also causes inhibition of A* in the exporting cell. This is because M affects both cells equally (Fig. 5A, dotted arrows). Thus, intuitively it seems unlikely that such a system would generate cell-cell coupling.

However, computer simulations show that this indirect system can generate longitudinal coordination of cell polarities in a single file of cells, despite extracellular M acting equally on both membranes at each cell-cell interface (Fig. 5B). In these simulations, we assume that both intracellular and extracellular M diffuse rapidly compared with A* and B*, and that M is produced and degraded at uniform rates in all cells. We also assume that M can move across the cell membrane independently of polarity components, with a higher permeability for cell entry than exit. A cell that has been polarised through intracellular partitioning thus exports M at the A*-rich end and has a net passive import of M at other locations, giving a flow of M along its polarity. Because M flows in the same direction as the cell polarity, it tends to accumulate within cells at the end of the cell file to which the polarity points (right end in Fig. 5B). Thus, cells end up pointing towards a region with high intracellular M concentration.

To understand how polarity coordination arises with this system, consider a scenario in which all cells have their polarity aligned except for one cell, labelled R in Fig. 5C, which has opposite polarity compared with the others. In this situation, extracellular space at the A* end of the R cell (left end) has high concentrations of extracellular M, because it is flanked on both sides by A*-rich membranes (and A* promotes export of M). These high levels of extracellular M diminish A* at this end of the R cell (as M inhibits A*), as well as along the adjacent membrane of its left neighbour. The other end of the R cell (right end) has low levels of extracellular M because M is transported away from the extracellular space on both sides. Low levels of M favour A*, both along the right membrane of cell R, as well as along the adjacent membrane of its right neighbour. Although cell R is in an unfavourable situation along both membranes, its flanking neighbours are only so along one of their membranes. Taken together, these processes would therefore be expected to reverse the polarity of the R cell alone, and thus align it with the other cells of the file.

An attractive feature of indirect cell-cell coupling is that it does not require reading of gradients in M across the thickness of the extracellular space or gradients of M in the cytoplasm along the length of the cell. Indeed, in our implementation of indirect cell-cell coupling, we assume that the level of M is uniform both within the cytoplasm of a cell and across the thickness of the extracellular space, although the system also works if gradients of M are allowed to form within cells. The mechanism of indirect cell-cell coupling we present requires intracellular partitioning: if A* and B* do not auto-activate and cross-inhibit then cells have no polarity (Fig. 5D).

The same indirect cell-cell coupling model applied to a 2D array of cells leads to locally coordinated groups of cells, or swirled patterns of orientations, which are both laterally and longitudinally coordinated (Fig. 5E). Thus, the outcomes of indirect and direct cell coupling are comparable (compare Fig 4H with Fig. 5E).

The model of indirect cell-cell coupling arises naturally from the intracellular partitioning-based framework presented here and may be of particular relevance to plants. This is because the plant cell wall is a major barrier to direct interactions between proteins in the plasma membranes of adjacent cells. (There are channels through plant cell walls, called plasmodesmata, but it is currently unclear

whether they play a role in control of tissue cell polarity.) Thus, cell-cell coupling in both plant and animal systems can be viewed as different elaborations of a common underlying system. By contrast, it is unclear how previous models, which do not incorporate intracellular partitioning (e.g. Burak and Shraiman, 2009), could be extended to both systems.

Organising polarity across a tissue

In many cases, cell polarity is coordinated across a large domain of tissue, such as a wing or leaf. Moreover, this polarity is related to the overall morphology of the structure, such as its proximodistal axis. Such organisation suggests that there are reference regions in the tissue that actively influence polarity and from where polarity information propagates. We refer to these reference regions as 'tissue polarity organisers' (Green et al., 2010). The term organiser has been used in several developmental contexts (e.g. Spemann and Mangold, 1924; Sabatini et al., 1999) but here we use it specifically in relation to the coordination of tissue cell polarity. Because cell polarity can be influenced to point away from or towards organisers, it is convenient to refer to two types of tissue cell polarity organiser, plus (+) or minus (–) respectively, according to their resultant effect on polarity. Although regions of organiser activity are often expected to be associated with sites of polarity divergence (+) or convergence (–), such polarity patterns are not sufficient to infer the presence of an organiser because they may also arise through polarity propagation from organisers located elsewhere. There are various mechanisms by which tissue cell polarity organisers may influence cell polarity over an extended domain. These mechanisms need not be mutually exclusive. We first consider direct modulations of polarity components, then tissue gradients and finally modulation of mediator levels for systems with indirect cell-cell coupling.

Direct modulation of polarity components

Cell-cell coupling together with intracellular partitioning generates swirls of polarity in a 2D array of cells (Fig 4H, Fig. 5E). To produce polarity that is coordinated with respect to the tissue, polarity components of this system can be modulated at tissue boundaries. With direct cell-cell coupling, for example, expression of only A and A* in a column of cells at the left boundary of the tissue and only B and B* in a column at the right boundary, results in a pattern in which polarity points from left to right across the tissue (Fig. 6A). The presence of only A* in leftmost cells causes B* to be elevated in the juxtaposed membrane of their right neighbours, through cell-cell coupling, giving the neighbours a rightwardly oriented polarity (cell polarity points from the B*-rich to the A*-rich end). The same effect then propagates through cell-cell coupling to the cells further along to the right. Similar considerations apply to the right boundary expressing only B*. One limitation of using direct modulation of polarity components as organisers of tissue polarity is the restricted range over which polarity is coordinated (Burak and Shraiman, 2009).

We may simulate the effect of introducing mutant patches into this model, as these predict patterns that can be evaluated experimentally through creation of clones (Lawrence et al., 2007). When mutant patches are introduced, polarity reversals are generated in the surrounding tissue. For example, a mutant patch that lacks A* (and thus only expresses B*) exhibits polarity reversal towards the right end of the patch (Fig. 6B). The patch is effectively acting as a minus organiser. The outer cell border within the mutant patch exhibits inwardly oriented polarities with respect to B* concentrations (polarity points away from the B*-rich end).

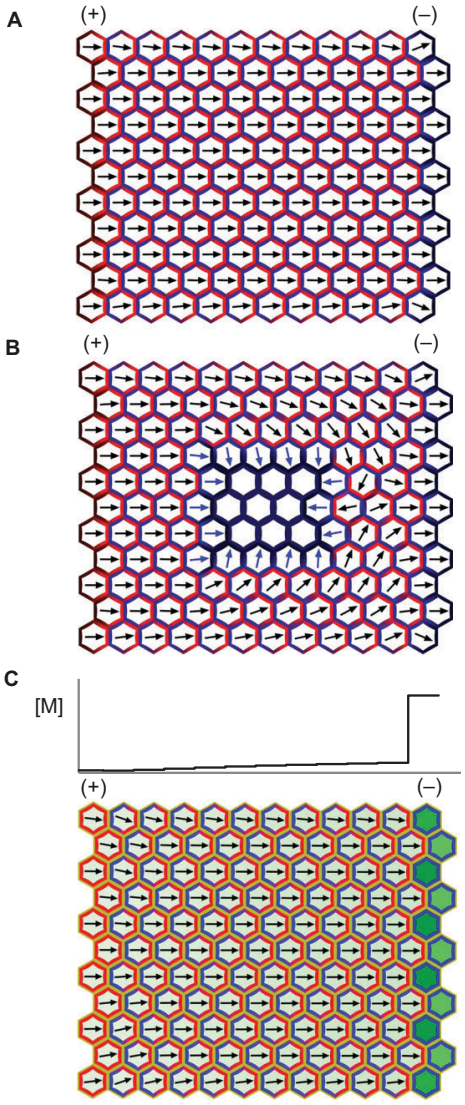

Fig. 6. Tissue polarity organisers that act through direct modulation of polarity components. (**A**) A file of cells on the left expressing only A and A* [plus (+) organiser] and a file on the right expressing only B and B* [minus (–) organiser], along with direct cell-cell coupling, leads to an organised left-right polarity pattern across the tissue. Polarity in cells expressing only one polarity component is shown with respect to that polarity component. (**B**) A mutant patch of cells lacking A and A* causes polarity reversal of wild-type tissue surrounding the right end of the patch (direct cell-cell coupling). (**C**) As for panel A but with indirect cell-cell coupling. Graph shows the concentration of intracellular M per cell for a single row of cells in the grid. The concentration of intracellular M is also indicated by the intensity of green within each cell in the grid.

This is because the A* in the wild-type neighbours draws B* in mutant border cells towards them through cell-cell coupling. The resulting inwardly oriented polarity of mutant cells is restricted to cells on the border of the patch, as cells further in do not have neighbours with A*.

For indirect cell-cell coupling, polarity coordination may arise in a similar manner (Fig. 6C). In this case, coordination arises because cells at the left boundary, which express only A*, export M at all locations around their membranes (A* promotes M export), whereas cells at the right boundary only import M (because they lack A*). This creates a high level of extracellular M

at the left boundary of the tissue and a low level at the right boundary. This situation favours A* at the right end of the cells near the boundaries (extracellular M inhibits A*), biasing the orientation of polarity to point rightwards. The level of intracellular M becomes high in the minus organiser at the right boundary, because cells continually pump M towards it.

Tissue gradients

Another way of coordinating tissue cell polarity is through concentration gradients. Suppose we have a concentration gradient along a single file of cells for a signalling molecule S (Fig. 7A). In principle, the distribution of S carries two types of information. One is the gradient along the length of each cell, as each cell has a higher concentration of extracellular S at its left compared with its right end (Fig. 7B). We refer to this as a cellular gradient. The other type of information is the gradient between cells: the average concentration of S surrounding a cell is higher than that for its right neighbour and lower than that for its left neighbour (Fig. 7C). We refer to this as an intercellular gradient. We next consider how the cellular and intercellular aspects of the S gradient may lead to coordinated polarity for 2D cell arrays.

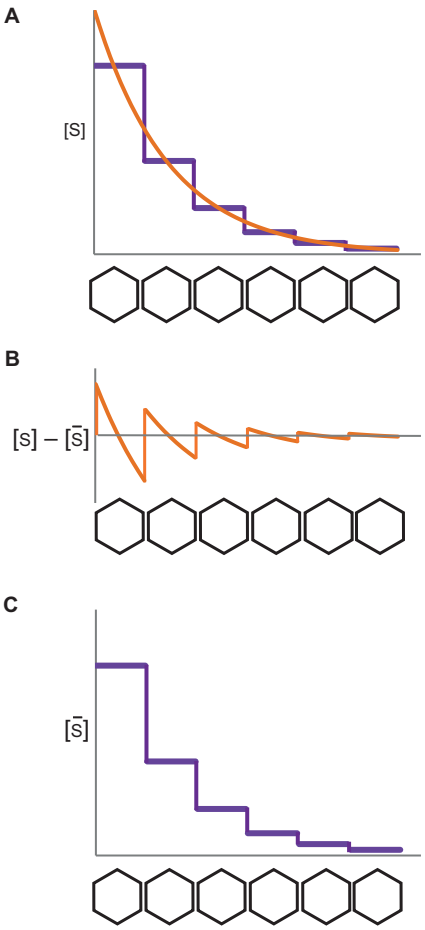

Fig. 7. Two aspects of a concentration gradient. (**A**) The information in a gradient in [S] across a tissue (orange) can be broken down into two separate types (B and C). (**B**) The cellular gradient (orange line) is displayed by plotting the difference between the concentration of S ([S]) at a given point along a cell and the mean concentration of S surrounding that cell ([S̄]), i.e. ([S]-[S̄]). (**C**) The intercellular gradient (purple line) is displayed by plotting the mean concentration of S surrounding a cell ([S̄]).

Cellular gradients

We begin with an array of cells with an intracellular partitioning system but no cell-cell coupling. S is produced at a high rate by the leftmost cells, degraded at a high rate by the rightmost cells, and diffuses in the extracellular space producing a left-to-right graded decline in S concentration. Assume that the concentration of S at each location in the extracellular space can be sensed through a membrane-bound receptor for which S is a ligand, and that triggering of the receptor promotes local conversion of A to A*. According to this system, each cell within the array will tend to have more A* in the membrane at its left end, relative to its right end, because of the gradient in S across the cell. This will bias the intracellular partitioning process such that the A*-rich end will form at the left of all cells. Because the gradient in S across the cell has the same orientation for all cells, cell polarities are oriented leftwards throughout the tissue, pointing up the S gradient (Fig. 8A). In this case, the left boundary cells producing S at a high rate serve as the minus organiser, whereas the right boundary where S is degraded at a high rate acts as a plus organiser.

With this system, coordination of polarity depends on the extent to which concentration gradients of S are aligned between cells. Polarity components are not directly involved in tissue coordination and thus act cell-autonomously. A patch that lacks A*, for example, does not influence the polarity of the surrounding wild-type cells and the cells within the patch have no polarity (Fig. 8B). By contrast, a mutant patch with a high degradation rate of S will influence the polarity of the tissue surrounding it by influencing neighbouring cellular concentration gradients (Fig. 8C). The gradient across cells near the right end of the patch will be reversed because they are adjacent to a region with low S concentration. As this mechanism depends on cellular gradients in S, it may become less effective for larger tissues as the gradient becomes shallow.

The above analysis assumes that cellular gradients in S act on a system with intracellular partitioning but no cell-cell coupling. If the system incorporates cell-cell coupling, similar results are obtained, except that a mutant patch lacking A* shows polarity reversal (at its left end, Fig. 8D). In addition, incorporation of cell-cell coupling allows coordinated polarity to extend further into the regions where the gradient in S is shallow (data not shown).

Intercellular gradients

Consider a case in which extracellular S is graded across the tissue and that it promotes production of a factor, F, within each cell, in proportion to the total level of S in the cell surroundings. In this case, the gradient in extracellular S leads to a stepped response, corresponding to the level of F in each cell. F is uniform within each cell but is graded across the tissue so that each cell has a higher level of F than its right neighbour, forming an intercellular gradient (Fig. 9A). Suppose that F within a cell increases production of the A polarity component above a basal rate of F-independent production. For example, F might be a transcription factor involved in generating A. In this situation, a higher level of F in the cell leads to raised levels of both A and A* (the concentration of A* is dependent on A). Thus, each cell has a neighbour to its left with a slightly higher overall concentration of both A and A* (except for cells at the left boundary, which have no left neighbours). If we assume this promotion of A levels operates in a system with direct cell-cell coupling, the slight excess of A* in the left neighbour will tend to bias B* towards the left of the cell. Polarity will therefore be coordinated to point left to right (from B*-rich to A*-rich ends) across the tissue (lateral and longitudinal coordination). Thus, even in the absence of intracellular gradients in F, an organised pattern of

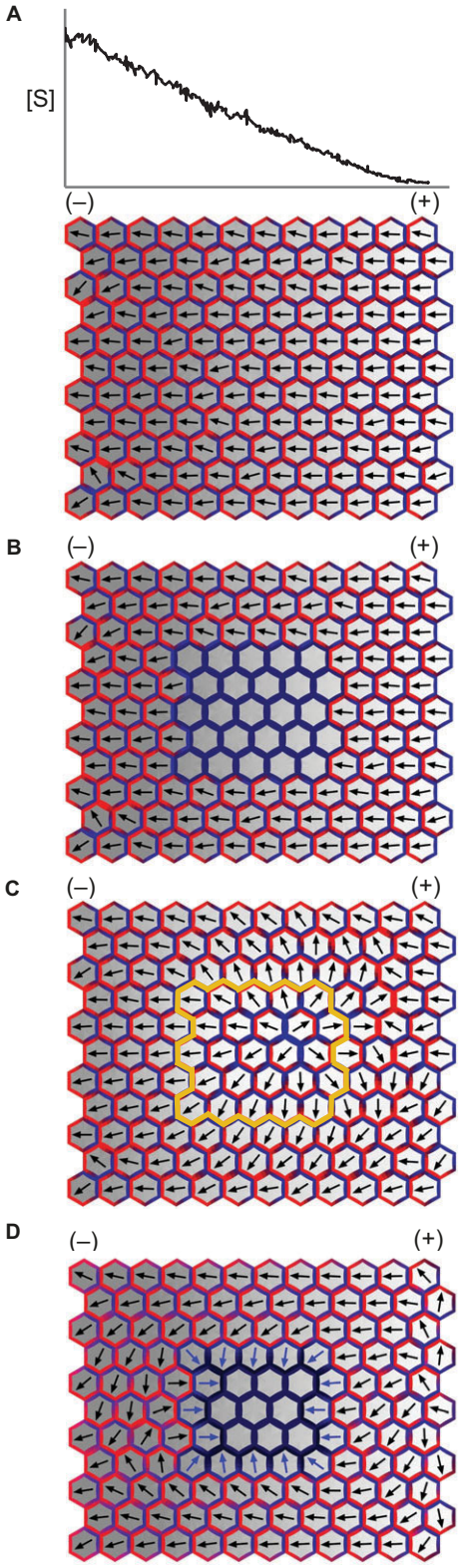

Fig. 8. Tissue cell polarity through cellular gradients. (**A**) Signalling factor S is produced at a high rate in the column of cells at the left boundary [minus (–) organiser] and degraded in the column on the right boundary [plus (+) organiser] and diffuses in the extracellular space. Small fluctuations in the concentration of S are also incorporated, yielding a noisy gradient. Extracellular S is detected in the membrane and promotes conversion of A to A*, leading to an organised right-left polarity pattern across the tissue. The graph displays extracellular S concentration, plotted against the position along the *x*-axis, for a single row of cells in the grid. Intensity of grey within each cell indicates the extracellular [S]. (**B**) A mutant patch lacking A and A* does not interfere with the polarity of the surrounding wild-type tissue because of the absence of cell-cell coupling. Cells within the mutant patch are not polarised. (**C**) A mutant patch with a high degradation rate of S (patch outlined in yellow) causes polarity reversal in cells surrounding the right of the patch. (**D**) In a system where cellular gradients are combined with direct cell-cell coupling, a mutant patch lacking A* shows polarity reversal at its left end.

tissue cell polarity emerges (Fig. 9A). In contrast to the cellular gradient mechanism, in this case a high level of S (and thus F) corresponds to a plus organiser whereas a low level corresponds to a minus organiser, even though in both cases S is enhancing A* (compare polarity orientations in Fig. 8A and Fig. 9A). A mutant patch that lacks A* causes polarity reversal at its right end (Fig. 9B). The outer cell border within the mutant patch exhibits inwardly oriented polarities with respect to B* concentrations, as described earlier (Fig. 6B and Fig. 8D). Similar results have been obtained with other direct cell-cell coupling models (Le Garrec et al., 2006; Burak and Shraiman, 2009).

Modulating mediator levels

For systems based on indirect cell-cell coupling, tissue cell polarity organisers may also act by influencing mediator (M) production or degradation. If M is produced at a higher rate in the column of cells at the left boundary and degraded at a higher rate in the column at the right, then polarity can become organised across the tissue, pointing from left to right (lateral and longitudinal coordination, Fig. 10A). This coordination partly arises because the gradient in extracellular M across the cells, generated by non-directed transport, inhibits A* at the left end of each cell, biasing polarity. However, in the absence of indirect cell-cell coupling this would only coordinate polarity of cells near the boundaries, as shown in simulations in which A* does not affect export of M (Fig. 10B). Incorporation of indirect cell-cell coupling then allows this coordination to propagate through the tissue (Fig. 10A). In this situation, the leftmost column of cells is acting as a plus organiser while the rightmost column acts as a minus organiser.

According to this model, the plus organiser corresponds to a region that produces M at a high rate while the minus organiser corresponds to a region that degrades M. The steady-state intracellular level of M is high in plus organiser regions and low in minus organiser regions. If the degradation rate of M in the right file is not sufficiently high, then M can accumulate in the rightmost column of cells through transport. This accumulation in turn leads to high levels of extracellular M at the right boundary, which may lead to polarity disruption as the cells at the right boundary switch from being sinks to sources of M (Fig. 10C). This effect may be counteracted if cells in the rightmost column are unable to export M (e.g. the lack A*, Fig. 10D). In this situation, the cells on the right can accumulate intracellular M through transport towards them, while their extracellular M is kept low because of the higher permeability of cells to M entry than M exit. Thus, the plus organiser at the left boundary now has low levels of intracellular M as it has a high net rate of M influx, whereas the minus organiser at the right boundary has high levels of intracellular M as it imports M at a high rate. A similar result is obtained if cells at the right boundary import M at a higher than basal rate, instead of exporting M at a reduced rate.

In all cases, M flows along the direction of polarity, but it can appear to flow either to a region with high intracellular M

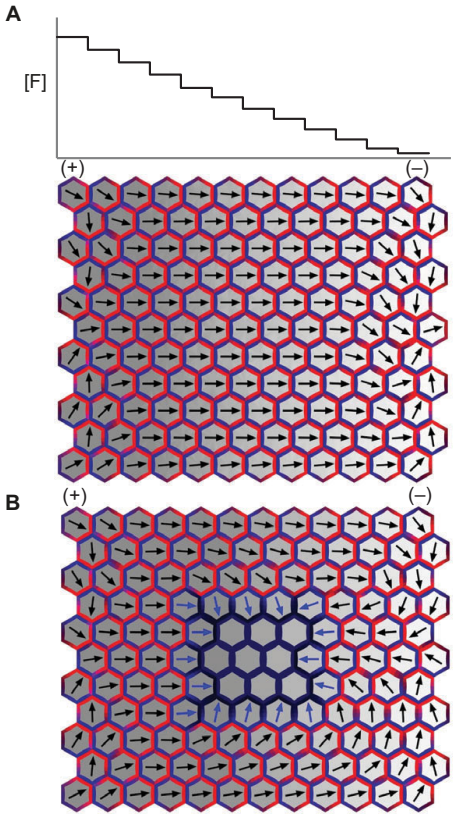

Fig. 9. Organisation of tissue cell polarity through intercellular gradients. (**A**) A signalling factor S is produced at a high rate in cells at the left boundary [plus (+) organiser] and degraded at the right boundary [minus (–) organiser]. S promotes production of a factor, F, within each cell, in proportion to the total level of S in the cell surroundings, creating an intercellular gradient of F across the tissue. The graph displays the concentration of F per cell for a single row of cells in the grid. The intensity of grey within each cell indicates the concentration of F. F promotes the total levels of A (A plus A*), and the intercellular gradient in A* leads to an organised left-right polarity pattern across the tissue. The cells near the left and right boundaries of the tissue deviate and do not have a clear left-right polarity orientation because these cells have no neighbours to one side. (**B**) A mutant patch unable to make A* causes polarity reversal in wild-type tissue surrounding the right border of the patch.

concentration (Fig 5B; Fig. 10D) or low intracellular M concentration (Fig. 10A), depending on whether organisers influence production and degradation of M and/or export and import of M.

Effects of cell geometry

Our simulations for single cell files show that cell-cell coupling provides an effective mechanism for longitudinal coordination of polarity (Fig. 4D,E; Fig. 5B). However, analysis of 2D arrays shows that cell-cell coupling also generates a degree of lateral coordination, illustrated by swirled patterns of polarity (Fig. 4H; Fig. 5E). Lateral coordination may arise because cells are not organised in distinct files in the 2D arrays, but are interlaced. To test this idea, we applied cell-cell coupling to a 2D array comprising a grid of square cells. With this cellular configuration, broad swirls of polarity are no longer observed (Fig. 11A,B). Instead, polarity can be coordinated longitudinally along single cell files, with lateral neighbours often showing opposite polarities as this pattern maximises contact between A* and B* in neighbours. However, in contrast to coordination systems based on cell-cell coupling, those involving intracellular partitioning combined with cellular gradients (Fig. 8A-C) are relatively insensitive to cell geometry (Fig. 11C). This is because cell polarity orientation is determined by cell-autonomous reading of the gradient in S and is thus independent of cell neighbours.

These simulations illustrate the effect of cell shape and configurations on cell-cell coupling mechanisms in regular arrays. However, in many biological situations, cells do not have completely regular geometries and sizes. Irregularities are inevitable during periods of cell proliferation if cells divide asynchronously and do not rearrange rapidly. If we apply cell-cell coupling systems to a grid of cells with irregular shapes, both lateral and longitudinal coordination still occur, as evidenced by swirled patterns, but are less effective than with hexagonal cells using the same parameters (Fig. 11D,E, compare with Fig. 4H; Fig. 5E). Similar effects of lattice disorder on polarity coordination have been described for other models that invoke cell interface interactions (Ma et al., 2008). With irregular cell geometries, organisers of tissue polarity lead to polarity coordination, although this is less effective than for hexagonal cells (Fig. 11F- I, compare with Fig. 6A,C; Fig. 9A and Fig. 10A).

Summary of theoretical analysis

The examples described above show how the intracellular partitioning-based framework provides a possible explanation for the generation of tissue cell polarity in plants and animals. Intracellular partitioning alone provides a mechanism for generating individual cell polarity in the absence of asymmetric cues. This establishes a ground state of randomly oriented polarities. This process may be modified by incorporating cell-cell coupling, which leads to local alignment of polarities. We show that cell-cell coupling can operate both directly, through membrane-spanning complexes, or indirectly, through mediator molecules. Incorporation of cell-cell coupling can lead to coordination of polarity across a tissue by selective expression of polarity components in boundary domains. Tissue coordination may be further enhanced through tissue gradients, which may operate at the cellular and/or intercellular level. Several of these mechanisms may act synergistically to establish and maintain polarity over extended domains. These systems can coordinate polarity for tissues with irregular cell geometries generated by cell division and growth, although coordination is less consistent than for regular hexagonal arrays.

Canonical examples from plants and animals

To illustrate how the framework outlined above can be used in different contexts, we apply it to some well-studied examples in animals and plants.

PCP in *Drosophila*

One of the best-studied tissue cell polarity systems in animals involves polarised orientation of hairs or bristles in *Drosophila* (Goodrich and Strutt, 2011). The *Drosophila* wing, for example, comprises two juxtaposed sheets of cells, with each cell producing a distally pointing hair near its distal vertex. Several mutants, such as *frizzled* (*fz*) and *Van Gogh* (*Vang*, also known as *strabismus*) have been identified that disrupt this coordinated pattern. Evidence that these genes play a role in polarity coordination comes from analysis of clonal patches of mutant tissue. Such patches exhibit reversal of polarity for a few rows of wild-type cells at one end of the clone. In some cases, such as fz^{-} clones, polarity is reversed at the distal end of the clone; in other cases, such as $Vang^{-}$ clones, polarity is reversed at the proximal end of the clone. Fz is a seven-pass transmembrane protein and is localised to the distal end of

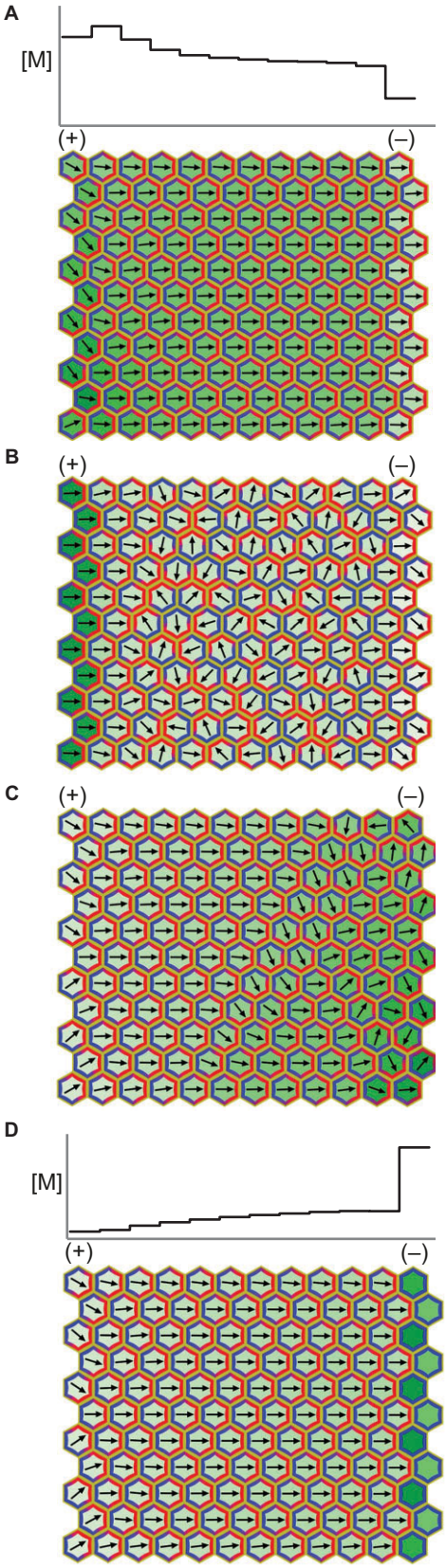

Fig. 10. Tissue coordination of polarity by modulation of M levels. (**A**) With an indirect cell-cell coupling system, a high production rate of M in the leftmost column of cells, combined with a high degradation rate in the rightmost column, biases the orientation of polarity across the tissue. The graph shows the concentration of intracellular M per cell for a single row of cells of the array. The intensity of green within cells indicates the concentration of intracellular M. (**B**) Same as panel A but A* does not promote export of M. Polarity is aligned only near the left and right borders. (**C**) If the degradation rate of M at the rightmost column is not sufficiently high relative to the production rate in the leftmost column, then M can accumulate at the right boundary of the tissue, causing disruption and instability of polarity coordination. (**D**) Combining the production and degradation rates used in C with removal of A* in the rightmost column of cells restores coordinated polarity. In this case, intracellular M concentration is highest in the rightmost column of cells [minus (–) organiser].

developing wing cells, whereas Vang is a four-pass transmembrane protein and is localised at the proximal end. These proteins interact with cytosolic proteins that also show polarised distributions: Dishevelled (Dsh) and Diego (Dgo) are localised at the distal end; and Prickle (Pk) is localised at the proximal end. In addition to these components, a seven-pass transmembrane cadherin protein Flamingo [Fmi, also known as Starry Night (Stan)] is present at both proximal and distal ends. Fmi most likely acts as a bridge between complexes on membranes of neighbouring cells (Usui et al., 1999; Lawrence et al., 2004; Strutt and Strutt, 2007). These six proteins (Fz, Vang, Dsh, Dgo, Pk and Fmi) have been placed in the same pathway: the core PCP pathway (Strutt and Strutt, 2009).

The observation of polarity reversals in the tissue surrounding mutant patches suggests that the core PCP genes are involved in one or more aspects of polarity coordination. In principle, they could encode components of a cell-cell coupling system (Fig. 9B), or be involved in enhancing degradation or production of a signalling molecule S (Fig. 8C). Two findings support their participation in cell-cell coupling. First, pathway components have polarised cellular locations. Such a localisation is expected if they are polarity components but not if they are involved in production or degradation of S. Second, reorientation of polarity occurs within *fz*$^{-}$ mutant tissue in a single cell layer that abuts Fz-expressing tissue (Lawrence et al., 2004), as expected for cell-cell coupling models, in which mutant regions contain a single layer of polarised cells (Fig. 6B; Fig. 8D; Fig. 9B). By contrast, there is no expectation that polarity would extend for only a single cell if Fz influenced the level of S, as a change in the gradient of S could, in principle, extend over several cells.

Several models based on direct cell-cell coupling have been proposed for how the core PCP pathway operates. These models have been designed to account for the observed polarity patterns in mutants, clonal patches, protein localisation and protein interactions. However, the formal relationships between the models have been unclear because each model has been presented as an individual solution. We next view these models through the framework described here so as to highlight their essential features (i.e. whether they involve intracellular partitioning, cell-cell coupling, cellular or intercellular gradients) and clarify experiments that might distinguish between them.

One model invokes interface interactions combined with intracellular bias (Amonlirdviman et al., 2005). Complexes are formed at each end of the cell, corresponding to the A* and B* components in the framework presented here. The A* complex involves Fz and Dsh, whereas the B* complex involves Vang and Pk. There is a bias in each cell such that higher levels of the A* complex are promoted at the distal end. Formation of the A* complex in one membrane promotes formation of the B* complex in the juxtaposed membrane of the neighbouring cell via

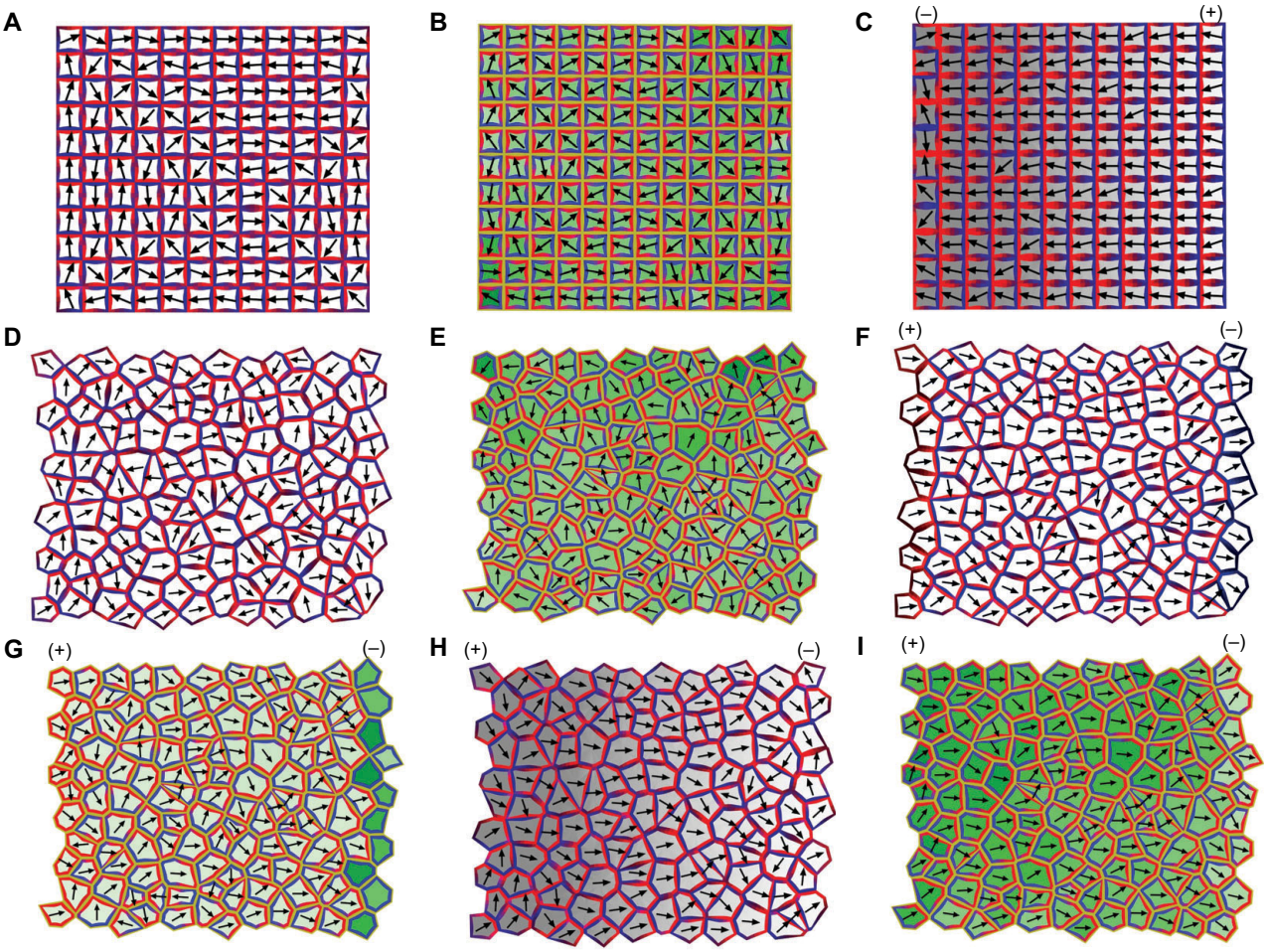

Fig. 11. Cell-cell coupling on grids of square or irregular cells. (**A**,**B**) Cell-cell coupling produces longitudinal coordination on a grid of square cells but lateral neighbours often have oppositely oriented polarities. This is the case with direct cell-cell coupling (A) and indirect cell-cell coupling via M (B). For B, the intensity of green shows the concentration of intracellular M per cell. (**C**) Cellular gradients combined with intracellular partitioning without cell-cell coupling produces both lateral and longitudinal coordination for a grid of square cells. The file of cells on the left [minus (–)] organiser has disorganised polarity because the gradient in S across these cells is shallow. (**D**,**E**) Cell-cell coupling is less effective at establishing lateral and longitudinal coordination in a grid of irregular cells. This is the case with direct cell-cell coupling (D) and indirect cell-cell coupling (E). (**F**,**G**) Organisers based on modulation of polarity components combined with direct cell-cell coupling (F) or indirect cell-cell coupling (G) lead to coordination of polarity for an irregular grid, although it is less consistent than for hexagonal cells (compare with Fig. 6A and6C). (**H**) Polarity coordination resulting from intercellular gradients combined with direct cell-cell coupling (compare with Fig. 9A). (**I**) In the case of indirect coupling, production of M in the leftmost cell column [plus (+) organiser] and its degradation in the rightmost cell column (minus organiser) leads to good polarity coordination, although again not quite as consistent as for hexagonal cells (compare with Fig. 10A).

interactions between Fz and Vang. Antagonism between A* and B* is mediated by B components Pk and Vang, which inhibit the formation of A* (Dsh binding to Fz). This system is equivalent to having direct cell-cell coupling combined with cellular gradients.

A second model involves cell interface interactions combined with a ligand that is high at the proximal end of the wing and declines distally (Le Garrec et al., 2006). The ligand is graded both along the length of each cell and between cells, and is needed to activate Fz, which then interacts with other components (Dsh, Dgo and Fmi) to generate A*. A* in the membrane of one cell can form a complex with B* (Vang, Pk, Fmi) in the juxtaposed membrane of the neighbouring cell via Fmi bridges. All polarity components can diffuse, except for the bridged A*-B* complex. Inhibition between A* and B* is mediated by A components (Dsh and Fz) that inhibit formation of fully active B* (Vang, Pk, Fmi). With the parameters used in the model, the intercellular gradient in the ligand leads to a Fz-containing complex being localised distally within each cell. This system is equivalent to direct cell-cell coupling combined with intercellular gradients.

A third model for PCP in *Drosophila* involves membrane-spanning complexes, with one orientation of the complex across the membrane (A*-B*) inhibiting formation of complexes with the opposite orientation (B*-A*) (Burak and Shraiman, 2009). There is an inhibitory messenger molecule (C*) that diffuses within each cell, creating an effective repulsion between the two possible orientations of the complex when cells have neighbours, thus ensuring that they become localised to the opposite ends of a cell. Tissue coordination is generated most effectively by an intercellular gradient. This model is also equivalent to direct cell-cell coupling combined with intercellular gradients.

The first two models assume that polarity is generated in the context of gradients across or between cells (Amonlirdviman et al., 2005; Le Garrec et al., 2006). Cells would therefore be expected to be unpolarised with respect to the PCP proteins in the absence of

asymmetric cues, such as ligand or expression gradients. Thus, individual cell polarity is fully dependent on global gradients across the tissue. This dependency does not apply in the case of the third model, because this mechanism generates swirls of polarity in the absence of a global orienting signal (Burak and Shraiman, 2009). However, with this model there is still a strong dependency on neighbours, as a cell cannot become polarised unless its neighbours are polarisable. Thus, it should not be possible, experimentally, to produce a single polarised cell. A further step towards independence from neighbours is given by the models described here. These systems have the potential to produce single polarised cells through intracellular partitioning, even when neighbours lack the ability to polarise (Fig. 4G). Each of these models could operate for *Drosophila* PCP, but they can be distinguished experimentally by testing the extent to which polarisation of individual cells depends on neighbours and global gradients.

All of the above models involve direct cell-cell coupling, but a seemingly different type of model has been proposed based on cell-cell comparisons (Adler et al., 1997; Lawrence et al., 2004). According to this model, cells compare levels of Fz activity with their neighbours, via Fmi bridges, and orient polarity so as to point to the neighbour with lowest Fz activity. However, this model does not provide an explicit mechanism for how cells are able to compare Fz concentrations with their neighbours, or how individual cell polarity is established and becomes aligned with the Fz activity gradient. As shown in our theoretical analysis and by others (Le Garrec et al., 2006; Burak and Shraiman, 2009), the combination of direct cell-cell coupling and intercellular tissue gradients can lead to cells orienting polarities according to differences in the level of polarity components (i.e. the level of A*, Fig. 9). The system behaves as if cells are comparing levels with neighbours and orienting their polarity accordingly. However, this behaviour is not an explicit input to the model but an outcome of molecular interactions. Thus, cell-cell comparison models can be seen as a different level of description rather than being contradictory to direct cell-cell coupling models.

A further complication with evaluating models is that the core PCP genes do not provide the only polarity components. If they did, then mutants in these genes would be expected to produce cells that lack polarity. This result is observed with respect to the position in the cell where the hair initiates: complete loss of core PCP proteins leads to hairs initiating in the cell centre instead of distally (Wong and Adler, 1993). However, with regard to hair orientation, individual cell polarity is still evident in the mutants, as each cell hair does not point vertically out of the tissue plane but in a direction along the plane. Moreover, this individual cell polarity is still coordinated to some extent between neighbours, giving swirls or broad domains of alignment (Wong and Adler, 1993). These observations suggest that the polarity system has redundancy and does not only depend on the core PCP pathway. In tissues such as the abdomen, some of this redundancy reflects the operation of a second pathway, involving the Fat (Ft) and Dachsous (Ds) cadherin proteins (Lawrence et al., 2007). However, even double mutants that lack activity in both the core PCP and Ft/Ds pathways have hairs pointing along the plane of the tissue; they even show swirled organisation in some areas (Casal et al., 2006), indicating that further levels of redundancy are involved. In support of this conclusion, a *fz*-independent system based on septate junction proteins Gliotactin (Gli) and Coracle (Cora) has been described that is also involved in alignment of hair polarity (Venema et al., 2004).

A further question is how do organisers act to coordinate polarity over the tissue? For example, hairs point distally with respect to the *Drosophila* wing. This suggests that organisers are most likely to be located at the hinge region at the proximal edge of the wing and/or at the distal tip of the wing, which is defined by the intersection of the anteroposterior and dorsoventral compartment boundaries (see Goodrich and Strutt, 2011). Tissue boundaries are thus expected to be locations where polarity components are modulated, and/or sources or sinks of underlying tissue gradients. Wing cells exhibit irregular shapes at early stages when cells are still dividing (Classen et al., 2005). At these stages, PCP proteins, such as Vang, already show preferential orientations towards the wing margin (Aigouy et al., 2010). Thus, coordinated polarity of core PCP proteins occurs in the context of irregular cell geometries. Such coordination may arise through organisers that are based on the modulation of polarity components and/or tissue gradients (Fig. 11F,H).

Evidence for tissue gradients playing a role comes from analysis of planar polarity in the *Drosophila* eye. Cells in the eye become polarised through preferential distribution of the cadherin Ds (A*) to one cell end and its binding partner the cadherin Ft (B*) to the opposite cell end (Ambegaonkar et al., 2012; Brittle et al., 2012). Planar polarity patterns are specified by opposite gradients in expression of Ds and the Golgi-associated protein Four-jointed (Fj) (Simon, 2004). Fj expression is highest at the equator whereas Ds expression is highest at the pole. As these transcriptional gradients operate through the nucleus, they act at the intercellular level. As shown in Fig. 9, an intercellular gradient in A* levels is expected to orient polarity such that the B*-rich end of the cell is oriented towards regions with higher A* expression. This is consistent with the observation that Ft-rich (B*-rich) ends are oriented towards regions with higher Ds (A*) expression at the pole. Fj has been proposed to modify Ft or Ds so that the ability of Ft (B*) to form intercellular bridges is enhanced relative to Ds (A*) (Brittle et al., 2010; Simon et al., 2010). Thus, the expression gradient in Fj is equivalent to an intercellular gradient in B* levels, and should orient the A*-rich end of the cell towards regions with higher B* (Fj) expression. Consistent with this expectation, Ds-rich ends are oriented towards regions with high Fj expression at the equator. The tissue gradients in Ds and Fj expression depend on graded distributions of morphogens, such as Wingless, that emanate from tissue and compartment boundaries. Thus, in terms of our framework, graded Wingless levels take the place of S, regulating the expression of Ds and of Fj.

PIN localisation in plants

The most intensively studied tissue cell polarity system in plants involves localisation of the PIN auxin efflux carriers (Křeček et al., 2009). Several PIN proteins, such as PIN1, PIN2, PIN3, PIN4 and PIN7, can exhibit coordinated polarised distributions within cells of particular tissues. For example, PIN1 in the root is located at the basal (rootward) end of vascular cells, whereas PIN2 is at the apical (shootward) end of epidermal cells (Blilou et al., 2005). PIN tissue cell polarity is also related to sites of high auxin concentration. Auxin maxima, for example, are observed at regions around which PIN polarities are orientated, such as the quiescent centre of the root tip and the centre of initiating leaf primordia (Blilou et al., 2005; Heisler et al., 2005). The PIN polarity pattern can also be influenced by application of auxin, suggesting that auxin may feed back to influence the polarity of the cells that transport it (Jönsson et al., 2006; Smith et al., 2006).

Several models have been proposed to account for how tissue cell polarity of PIN proteins is established. In one type of model, cells become polarised if they sense that their neighbours have different auxin concentrations. PIN proteins then become localised

to the cell end with the highest auxin level in its neighbour (Bayer et al., 2009; Jönsson et al., 2006; Smith et al., 2006; Sahlin et al., 2009). This leads to auxin flowing up intercellular auxin gradients. Such up-the-gradient cell-cell comparison models can account for observed PIN1 and auxin distributions, and spacing patterns between organ primordia (phyllotaxy). However, these models raise the question how do cells sense auxin levels in their neighbours or align their polarity accordingly? One possibility is that disparities in auxin concentrations between adjacent ends of neighbouring cells generate differential physical stresses in the cell wall between them. If the cell preferentially allocates PINs to its membranes next to walls under the highest stress (corresponding to those interfaces that have the highest auxin increase from the cell to its neighbour), PIN polarity would arise (Heisler et al., 2010).

In another type of model, cells become polarised if there is a flux of auxin across them. Cells detect the level of net auxin flux at cell-cell interfaces and localise PIN molecules to the membranes with maximum flux out of a cell (Rolland-Lagan and Prusinkiewicz, 2005; Stoma et al., 2008; Bayer et al., 2009). This leads to polarity being aligned with the direction of auxin flow. An advantage of these with-the-flux models is that they can account for observed venation patterns, as these arise through formation of channels of high auxin flux (canalisation). However, mechanisms for flux sensing remain to be identified.

An alternative model for aligning polarity with the direction of auxin flow is that cells detect auxin gradients across the thickness of cell walls through a diffusible auxin receptor, with a diffusion constant that is decreased by auxin binding (Wabnik et al., 2010). PINs are then preferentially localised to the membrane with the higher auxin signal. This model can also recapitulate observed patterns of PIN polarisation during formation of vasculature. However, it is unclear whether the candidate auxin receptor protein [ABP1 (Sauer and Kleine-Vehn, 2011)] has the required auxin-dependent mobility within a cell wall, and whether auxin gradients across the thickness of a cell wall would be sufficiently large, given the thinness of the wall and the high diffusion rate of auxin.

The intracellular partitioning-based framework presented here represents a further type of model for tissue cell polarity of PIN proteins. Unlike the above models, which assume that a cell does not become polarised in the absence of auxin gradients or flux across it, we propose that cells can become polarised even in the absence of asymmetries in auxin, through intracellular partitioning. Auxin then acts as a mediator, M, that coordinates polarities through indirect cell-cell coupling. As shown in the theoretical examples, if the A* component leads to enhanced PIN activity (M export) and extracellular auxin (M) inhibits A*, polarities become co-aligned with directions of auxin flow, similar to the outcome of with-the-flux models. According to the intracellular partitioning-based model, polarity points away from regions with high extracellular auxin (plus organisers) and towards regions with low extracellular auxin (minus organisers). However, the level of intracellular auxin need not correlate with these extracellular levels. Intracellular auxin can be high at a plus organiser because of high auxin production rates (Fig. 10A) or it may be high at a minus organiser because auxin may accumulate there through transport (provided that extracellular auxin is kept low; Fig. 6C, Fig. 10D). The latter outcome is consistent with polarities pointing towards regions with high expression of auxin-inducible gene markers, such as DR5 (Heisler et al., 2005). Thus, the intracellular partitioning-based model is equally compatible with observed PIN polarity patterns associated with up-the-gradient or with-the-flux models. There have been other approaches to reconciling these patterns using a unified mechanism (Bayer et al., 2009; Stoma et al., 2008; Merks et al., 2007). However, unlike these models, our model does not invoke cell-cell comparisons or measurements of flux. Our model also does not involve detection of stresses or detection of gradients across cell walls. Instead, alignments arise through the interplay between intracellular partitioning and auxin transport processes.

A distinctive feature of the model proposed here is that there is a separable mechanism for intracellular partitioning. Candidate components for intracellular partitioning are the Rho-GTPases, a family of small G-proteins that may be either membrane bound or cytosolic (Yang, 2008). The inactive form is released from the membrane and becomes cytosolic through interaction with guanine nucleotide dissociation inhibitor proteins (GDIs). In animals, polarity of migrating cells is associated with segregation of different members of the Rho-GTPase family, typically with high levels of active Rac and Cdc42 (equivalent to A*) at the front region of the cells and high levels of active Rho (e.g. B*) at the back region. Computational modelling has shown that this asymmetry can be accounted for through mutual inhibition of the A* and B* forms, together with faster diffusion of the cytosolic GDI-linked A and B forms (Marée et al., 2006; Jilkine et al., 2007). A similar model might underlie polarity of pavement cells in plants. Here, different members of Rho-like GTPases from plants, called ROPs, are thought to antagonise each other such that ROP2 (equivalent to A*) becomes localised to regions that form protrusions (lobes), while ROP6 (e.g. B*) becomes localised to indentation (Fu et al., 2005; Xu et al., 2010). As with the model for animal cells, the inactive cytosolic forms, which are associated with GDIs, play a key role in allowing the pattern to form.

If intracellular partitioning through ROPs is linked to tissue polarity with auxin acting as mediator, ROPs would be expected to influence auxin transport, while auxin levels should influence ROPs. Localisation of PIN1 is correlated with that of ROP2 and its effectors in pavement cell lobes, consistent with ROP2 enhancing local PIN1 levels and thus auxin export (Xu et al., 2010). Auxin has also been shown to activate ROPs within minutes through a local membrane-bound auxin receptor (ABP1), consistent with auxin feeding back to influence intracellular partitioning (Xu et al., 2010). Based on these findings, it is feasible that an indirect cell-cell coupling model could coordinate polarity between neighbouring pavement cells, where active ROP2 (A*) increases auxin efflux, through promoting functional PIN1 localisation. In this instance, indirect cell-cell coupling would apply to interdigitation between adjacent cells, but the principles are very similar to those described here for indirect cell-cell coupling as applied to tissue cell polarity.

Many aspects of our intracellular partitioning-based framework for plant tissue cell polarity remain to be explored and tested further. For example, the framework predicts that cells should be able to polarise in the absence of asymmetric cues. It has been shown that separation of plant cells by cell wall digestion and protoplast formation leads to a loss of asymmetric PIN1 localisation (Boutté et al., 2006), which could be taken as evidence against intracellular partitioning. However, it is unclear whether such treatments affect activity of polarity components and also whether polarity has indeed been fully lost, as PIN1 is not a determinant of intracellular partitioning but only a target that enables cell-cell coupling. Thus, further polarity markers and ways of generating cells in uniform environments are needed.

Another prediction is that polarity should point away from regions with high extracellular auxin. At first sight, this prediction seems inconsistent with experiments in which microdroplets containing auxin are applied to apical meristems (Bayer et al., 2009). PIN polarity is seen to converge towards the site of auxin

application, suggesting that polarity is being oriented up the extracellular auxin gradient. However, these experiments do not lead to the generation of polarity convergence points in new locations, but at positions at which primordia are about to emerge (I2 positions). It is therefore possible that auxin application is simply accelerating formation of a pattern that is nascent in the meristem, rather than specifying a new convergence point.

A further prediction concerns the effect of cell ablation. PIN polarity has been shown to be oriented away from sites of ablation in nearby cells (Heisler et al., 2010). The local effect of ablation is not disrupted by the auxin transport inhibitor NPA or by uniform application of external auxin; observations that have been taken to suggest that mechanical signals rather than auxin transport are responsible for coordinating PIN polarity (Heisler et al., 2010). An alternative explanation is that cell ablation causes an increase in extracellular auxin, which orients polarity according to the model described here. We show that, even in the absence of active efflux (i.e. when A* does not promote M export), coordination of polarity can extend over a few cells because of the gradient in extracellular auxin across the cells, generated by non-directed transport (left cells of Fig. 10B). Uniform application of external auxin need not disrupt polarity coordination as local gradients may still arise and be propagated through indirect cell-cell coupling.

A further test would be to determine whether polarity organisers act in the manner predicted. According to the intracellular partitioning-based framework, organisers correspond to regions where intracellular partitioning components or mediator (auxin) levels are modulated. This modulation could involve ROP/GDI activity, auxin biosynthesis (Zhao, 2010), auxin export (Křeček et al., 2009), auxin conjugation (Ludwig-Müller, 2011) or auxin import (Yang et al., 2006). These processes would therefore be targets of genes expressed in candidate regions of organiser activity, such as the root tip, base and tip of organ primordia, or base and tip of leaf serrations. Genes expressed in such boundary domains have been described and include *LATERAL SUPPRESSOR*, members of the NAC and LBD families and *PLETHORA* (Greb et al., 2003; Aida et al., 2004; Aida and Tasaka, 2006; Majer and Hochholdinger, 2011). It should be possible to test whether these genes influence polarity components and auxin distributions in a manner predicted by the intracellular partitioning-based framework.

In the framework for plant tissue polarity presented here, we make several simplifying assumptions. For example, we assume that all cells have the same level of PIN and that there is no feedback of intracellular auxin levels on PIN expression or auxin import. More elaborate models that incorporate modulation of PIN levels may allow the framework to be extended and account for patterns such as phyllotaxy, venation or reflux loops.

Concluding remarks

We show how tissue cell polarity may be established through an intracellular partitioning-based framework. Intracellular partitioning components can be modulated by incorporating interface interactions to produce cell-cell coupling that generates local alignment. Alignment across a tissue is established through tissue polarity organisers that are typically located at boundary regions. These organisers can act by modulating polarity components directly and/or through tissue gradients. We have shown how this framework can be applied to both animal and plant systems. A distinctive feature of animal cells is that molecules may bridge from one cell to another, allowing direct cell-cell coupling. Plant cells, however, are separated by cell walls, and polarities may be coupled more indirectly through transport of small mediator molecules such as auxin.

The intracellular partitioning-based framework allows different cell polarity systems to be placed in an evolutionary context. Cell polarity can be exhibited by individual cells in the absence of external molecular asymmetries (Wedlich-Soldner and Li, 2003). This is evident both for unicellular organisms, such as yeast (Johnson et al., 2011; Mogilner et al., 2012), and for individual cells from multicellular organisms, such as fish epidermal keratocytes (Verkhovsky et al., 1999; Marée et al., 2012) and isolated plant xylem cells (Oda and Fukuda, 2012). Thus, systems for generating intracellular partitioning are widespread and evolutionarily ancient, suggesting that they may provide a basic building block for establishing tissue polarity (Meinhardt, 2007). The tissue polarity mechanisms observed in plants and animals would then reflect the distinct constraints of each system during the evolution of multicellularity from unicellular ancestors, which already possessed intracellular partitioning systems. In animals, systems may have evolved in which individual cell polarities have become completely dependent on cell-cell interactions, so that intracellular partitioning no longer operates for a cell in isolation. These may represent evolutionary derived states, much as the mitochondria and chloroplasts may be viewed as derived states in which a prokaryote becomes completely dependent on its cellular host and no longer operates in isolation.

Many of the components and predictions of the intracellular partitioning-based framework remain to be tested. The framework thus provides a unifying and testable working hypothesis for tissue polarity that serves to guide further experimental and theoretical studies.

Acknowledgements

We thank Emily Abrash, Paul Adler, Desmond Bradley, Jordi Chan, Florent Patin, Jean-François LeGarrec, Xana Rebocho, Anne-Gaelle Rolland Lagan, Susana Sauret-Güeto and Georg Walther for helpful discussions and comments on the manuscript. We also thank Erika Kuchen for providing the image used in Fig. 1B.

Funding

The author's research was supported by the UK Biotechnology and Biological Research Council (E.C., A.B., A.F.M.M. and V.A.G.), a Wellcome Turst Senior Fellowship (to D.S.) and the Natural Sciences and Engineering Council of Canada (to P.P.). K.A. is supported by the Gatsby Charitable Foundation and V.A.G. acknowledges support from the Royal Society Dorothy Hodgkin Fellowship.

Competing interests statement

The authors declare no competing financial interests.

Supplementary material

Supplementary material available online at
http://dev.biologists.org/lookup/suppl/doi:10.1242/dev.062984/-/DC1

References

Adler, P. N., Krasnow, R. E. and Liu, J. (1997). Tissue polarity points from cells that have higher Frizzled levels towards cells that have lower Frizzled levels. *Curr. Biol.* **7**, 940-949.

Aida, M. and Tasaka, M. (2006). Morphogenesis and patterning at the organ boundaries in the higher plant shoot apex. *Plant Mol. Biol.* **60**, 915-928.

Aida, M., Beis, D., Heidstra, R., Willemsen, V., Blilou, I., Galinha, C., Nussaume, L., Noh, Y. S., Amasino, R. and Scheres, B. (2004). The PLETHORA genes mediate patterning of the Arabidopsis root stem cell niche. *Cell* **119**, 109-120.

Aigouy, B., Farhadifar, R., Staple, D. B., Sagner, A., Röper, J. C., Jülicher, F. and Eaton, S. (2010). Cell flow reorients the axis of planar polarity in the wing epithelium of Drosophila. *Cell* **142**, 773-786.

Ambegaonkar, A. A., Pan, G., Mani, M., Feng, Y. and Irvine, K. D. (2012). Propagation of Dachsous-Fat planar cell polarity. *Curr. Biol.* **22**, 1302-1308.

Amonlirdviman, K., Khare, N. A., Tree, D. R., Chen, W. S., Axelrod, J. D. and Tomlin, C. J. (2005). Mathematical modeling of planar cell polarity to understand domineering nonautonomy. *Science* **307**, 423-426.

Bayer, E. M., Smith, R. S., Mandel, T., Nakayama, N., Sauer, M., Prusinkiewicz, P. and Kuhlemeier, C. (2009). Integration of transport-based models for phyllotaxis and midvein formation. *Genes Dev.* **23**, 373-384.

Benková, E., Michniewicz, M., Sauer, M., Teichmann, T., Seifertová, D., Jürgens, G. and Friml, J. (2003). Local, efflux-dependent auxin gradients as a common module for plant organ formation. *Cell* **115**, 591-602.
Blilou, I., Xu, J., Wildwater, M., Willemsen, V., Paponov, I., Friml, J., Heidstra, R., Aida, M., Palme, K. and Scheres, B. (2005). The PIN auxin efflux facilitator network controls growth and patterning in Arabidopsis roots. *Nature* **433**, 39-44.
Boutté, Y., Crosnier, M. T., Carraro, N., Traas, J. and Satiat-Jeunemaitre, B. (2006). The plasma membrane recycling pathway and cell polarity in plants: studies on PIN proteins. *J. Cell Sci.* **119**, 1255-1265.
Brittle, A. L., Repiso, A., Casal, J., Lawrence, P. A. and Strutt, D. (2010). Four-jointed modulates growth and planar polarity by reducing the affinity of dachsous for fat. *Curr. Biol.* **20**, 803-810.
Brittle, A., Thomas, C. and Strutt, D. (2012). Planar polarity specification through asymmetric subcellular localization of Fat and Dachsous. *Curr. Biol.* **22**, 907-914.
Burak, Y. and Shraiman, B. I. (2009). Order and stochastic dynamics in Drosophila planar cell polarity. *PLoS Comput. Biol.* **5**, e1000628.
Casal, J., Lawrence, P. A. and Struhl, G. (2006). Two separate molecular systems, Dachsous/Fat and Starry night/Frizzled, act independently to confer planar cell polarity. *Development* **133**, 4561-4572.
Classen, A. K., Anderson, K. I., Marois, E. and Eaton, S. (2005). Hexagonal packing of Drosophila wing epithelial cells by the planar cell polarity pathway. *Dev. Cell* **9**, 805-817.
Fu, Y., Gu, Y., Zheng, Z., Wasteneys, G. and Yang, Z. (2005). Arabidopsis interdigitating cell growth requires two antagonistic pathways with opposing action on cell morphogenesis. *Cell* **120**, 687-700.
Goodrich, L. V. and Strutt, D. (2011). Principles of planar polarity in animal development. *Development* **138**, 1877-1892.
Greb, T., Clarenz, O., Schafer, E., Muller, D., Herrero, R., Schmitz, G. and Theres, K. (2003). Molecular analysis of the LATERAL SUPPRESSOR gene in Arabidopsis reveals a conserved control mechanism for axillary meristem formation. *Genes Dev.* **17**, 1175-1187.
Green, A. A., Kennaway, J. R., Hanna, A. I., Bangham, J. A. and Coen, E. (2010). Genetic control of organ shape and tissue polarity. *PLoS Biol.* **8**, e1000537.
Heisler, M. G., Ohno, C., Das, P., Sieber, P., Reddy, G. V., Long, J. A. and Meyerowitz, E. M. (2005). Patterns of auxin transport and gene expression during primordium development revealed by live imaging of the Arabidopsis inflorescence meristem. *Curr. Biol.* **15**, 1899-1911.
Heisler, M. G., Hamant, O., Krupinski, P., Uyttewaal, M., Ohno, C., Jönsson, H., Traas, J. and Meyerowitz, E. M. (2010). Alignment between PIN1 polarity and microtubule orientation in the shoot apical meristem reveals a tight coupling between morphogenesis and auxin transport. *PLoS Biol.* **8**, e1000516.
Jilkine, A., Marée, A. F. and Edelstein-Keshet, L. (2007). Mathematical model for spatial segregation of the Rho-family GTPases based on inhibitory crosstalk. *Bull. Math. Biol.* **69**, 1943-1978.
Johnson, J. M., Jin, M. and Lew, D. J. (2011). Symmetry breaking and the establishment of cell polarity in budding yeast. *Curr. Opin. Genet. Dev.* **21**, 740-746.
Jönsson, H., Heisler, M. G., Shapiro, B. E., Meyerowitz, E. M. and Mjolsness, E. (2006). An auxin-driven polarized transport model for phyllotaxis. *Proc. Natl. Acad. Sci. USA* **103**, 1633-1638.
Kramer, E. M., Frazer, N. L. and Baskin, T. I. (2007). Measurement of diffusion within the cell wall in living roots of Arabidopsis thaliana. *J. Exp. Bot.* **58**, 3005-3015.
Křeček, P., Skůpa, P., Libus, J., Naramoto, S., Tejos, R., Friml, J. and Zažímalová, E. (2009). The PIN-FORMED (PIN) protein family of auxin transporters. *Genome Biol.* **10**, 249.
Lawrence, P. A., Casal, J. and Struhl, G. (2004). Cell interactions and planar polarity in the abdominal epidermis of Drosophila. *Development* **131**, 4651-4664.
Lawrence, P. A., Struhl, G. and Casal, J. (2007). Planar cell polarity: one or two pathways? *Nat. Rev. Genet.* **8**, 555-563.
Le Garrec, J. F., Lopez, P. and Kerszberg, M. (2006). Establishment and maintenance of planar epithelial cell polarity by asymmetric cadherin bridges: a computer model. *Dev. Dyn.* **235**, 235-246.
Ludwig-Müller, J. (2011). Auxin conjugates: their role for plant development and in the evolution of land plants. *J. Exp. Bot.* **62**, 1757-1773.
Ma, D., Amonlirdviman, K., Raffard, R. L., Abate, A., Tomlin, C. J. and Axelrod, J. D. (2008). Cell packing influences planar cell polarity signaling. *Proc. Natl. Acad. Sci. USA* **105**, 18800-18805.
Majer, C. and Hochholdinger, F. (2011). Defining the boundaries: structure and function of LOB domain proteins. *Trends Plant Sci.* **16**, 47-52.
Marée, A. F., Jilkine, A., Dawes, A., Grieneisen, V. A. and Edelstein-Keshet, L. (2006). Polarization and movement of keratocytes: a multiscale modelling approach. *Bull. Math. Biol.* **68**, 1169-1211.
Marée, A. F., Grieneisen, V. A. and Edelstein-Keshet, L. (2012). How cells integrate complex stimuli: the effect of feedback from phosphoinositides and cell shape on cell polarization and motility. *PLoS Comput. Biol.* **8**, e1002402.
Meinhardt, H. (2007). Computational modelling of epithelial patterning. *Curr. Opin. Genet. Dev.* **17**, 272-280.
Merks, R. M. H., Van de Peer, Y., Inze, D. and Beemster, G. T. S. (2007). Canalization without flux sensors: a traveling-wave hypothesis. *Trends Plant Sci.* 12, 384-390.
Mitchison, G. (1980). A model for vein formation in higher plants. *Proc. R. Soc. B* **207**, 79-109.
Mogilner, A., Allard, J. and Wollman, R. (2012). Cell polarity: quantitative modeling as a tool in cell biology. *Science* **336**, 175-179.
Oda, Y. and Fukuda, H. (2012). Initiation of cell wall pattern by a Rho- and microtubule-driven symmetry breaking. *Science* **337**, 1333-1336.
Postma, M. and Van Haastert, P. J. (2001). A diffusion-translocation model for gradient sensing by chemotactic cells. *Biophys. J.* **81**, 1314-1323.
Postma, M., Bosgraaf, L., Loovers, H. M., and Van Haastert, P. J. (2004). Chemotaxis: signalling modules join hands at front and tail. *EMBO Rep.* **5**, 35-40.
Rolland-Lagan, A. G. and Prusinkiewicz, P. (2005). Reviewing models of auxin canalization in the context of leaf vein pattern formation in Arabidopsis. *Plant J.* **44**, 854-865.
Sabatini, S., Beis, D., Wolkenfelt, H., Murfett, J., Guilfoyle, T., Malamy, J., Benfey, P., Leyser, O., Bechtold, N., Weisbeek, P. et al. (1999). An auxin-dependent distal organizer of pattern and polarity in the Arabidopsis root. *Cell* **99**, 463-472.
Sachs, T. (1981). The controls of the patterned differentiation of vascular tissues. *Adv. Bot. Res.* **9**, 151-262.
Sahlin, P., Söderberg, B. and Jönsson, H. (2009). Regulated transport as a mechanism for pattern generation: capabilities for phyllotaxis and beyond. *J. Theor. Biol.* **258**, 60-70.
Sauer, M. and Kleine-Vehn, J. (2011). AUXIN BINDING PROTEIN1: the outsider. *Plant Cell* **23**, 2033-2043.
Simon, M. A. (2004). Planar cell polarity in the Drosophila eye is directed by graded Four-jointed and Dachsous expression. *Development* **131**, 6175-6184.
Simon, M. A., Xu, A., Ishikawa, H. O. and Irvine, K. D. (2010). Modulation of fat:dachsous binding by the cadherin domain kinase four-jointed. *Curr. Biol.* **20**, 811-817.
Smith, C., Prusinkiewicz, P. and Samavati, F. (2003). Local specification of surface subdivision algorithms (Applications of Graph Transformations with Industrial Relevance (AGTIVE 2003)). *Lecture Notes Comp. Sci.* **3062**, 313-327.
Smith, R. S., Guyomarc'h, S., Mandel, T., Reinhardt, D., Kuhlemeier, C. and Prusinkiewicz, P. (2006). A plausible model of phyllotaxis. *Proc. Natl. Acad. Sci. USA* **103**, 1301-1306.
Spemann, H. and Mangold, H. (1924). Über Induktion von Embryonalanlagen durch Implantation artfremder Organisatoren. *Arch. Mikr. Anat. und Entw. Mech.* **100**, 599-638.
Stoma, S., Lucas, M., Chopard, J., Schaedel, M., Traas, J. and Godin, C. (2008). Flux-based transport enhancement as a plausible unifying mechanism for auxin transport in meristem development. *PLoS Comput. Biol.* **4**, e1000207.
Strutt, D. and Strutt, H. (2007). Differential activities of the core planar polarity proteins during Drosophila wing patterning. *Dev. Biol.* **302**, 181-194.
Strutt, H. and Strutt, D. (2009). Asymmetric localisation of planar polarity proteins: Mechanisms and consequences. *Semin. Cell Dev. Biol.* **20**, 957-963.
Usui, T., Shima, Y., Shimada, Y., Hirano, S., Burgess, R. W., Schwarz, T. L., Takeichi, M. and Uemura, T. (1999). Flamingo, a seven-pass transmembrane cadherin, regulates planar cell polarity under the control of Frizzled. *Cell* **98**, 585-595.
Venema, D. R., Zeev-Ben-Mordehai, T. and Auld, V. J. (2004). Transient apical polarization of Gliotactin and Coracle is required for parallel alignment of wing hairs in Drosophila. *Dev. Biol.* **275**, 301-314.
Verkhovsky, A. B., Svitkina, T. M. and Borisy, G. G. (1999). Self-polarization and directional motility of cytoplasm. *Curr. Biol.* **9**, 11-20.
Wabnik, K., Kleine-Vehn, J., Balla, J., Sauer, M., Naramoto, S., Reinöhl, V., Merks, R. M., Govaerts, W. and Friml, J. (2010). Emergence of tissue polarization from synergy of intracellular and extracellular auxin signaling. *Mol. Syst. Biol.* **6**, 447.
Wedlich-Soldner, R. and Li, R. (2003). Spontaneous cell polarization: undermining determinism. *Nat. Cell Biol.* **5**, 267-270.
Wong, L. L. and Adler, P. N. (1993). Tissue polarity genes of Drosophila regulate the subcellular location for prehair initiation in pupal wing cells. *J. Cell Biol.* **123**, 209-221.
Xu, T., Wen, M., Nagawa, S., Fu, Y., Chen, J. G., Wu, M. J., Perrot-Rechenmann, C., Friml, J., Jones, A. M. and Yang, Z. (2010). Cell surface- and rho GTPase-based auxin signaling controls cellular interdigitation in Arabidopsis. *Cell* **143**, 99-110.
Yang, Z. (2008). Cell polarity signaling in Arabidopsis. *Annu. Rev. Cell Dev. Biol.* **24**, 551-575.
Yang, Y., Hammes, U. Z., Taylor, C. G., Schachtman, D. P. and Nielsen, E. (2006). High-affinity auxin transport by the AUX1 influx carrier protein. *Curr. Biol.* **16**, 1123-1127.
Zhao, Y. (2010). Auxin biosynthesis and its role in plant development. *Annu. Rev. Plant Biol.* **61**, 49-64.

APPENDIX S1. MODEL DESCRIPTIONS

Models were created using the VVe modeling environment, an extension of the VV system (Smith, 2003), which in turn is an extension of L-systems. During the implementation of all models, tissue is represented by a graph consisting of multiple vertices and edges (connections) between neighboring vertices. Each cell is represented by multiple vertices representing the cytoplasm and membrane. Details of tissue representations and the equations governing model behavior are given below for each model. Parameter values used in simulations, and the range of parameter values tested, are detailed in Table S1.

Intracellular partitioning

The intracellular partitioning system is used as a building block for all models. It involves interactions between rapidly diffusing inactive polarity components in the cytoplasm (A and B) and slowly diffusing, active polarity components in the membrane (A* and B*). We consider only the inter-conversion between A and A* (and B and B*), and thus assume a fixed total amount for each polarity component within a cell. This captures the fact that molecular switches typically interconvert on a much faster time scale than their regulated production or breakdown (Maree et al., 2006).

During the implementation of intracellular partitioning, tissue is represented by a graph containing two types of vertex: central vertices, which are positioned in the center of each cell, and peripheral vertices positioned around the perimeter of each cell (Fig. S1). All peripheral vertices of a cell are arranged to form a one dimensional closed region. Each peripheral vertex from the same closed region is connected to the central vertex of the same cell and to its immediately neighboring peripheral vertices of the same cell. Each peripheral vertex of a cell is also connected to the juxtaposed peripheral vertex of the neighboring cell, unless the vertex is on the border of the tissue.

In all models, the membrane of each cell is represented by peripheral vertices and the region of membrane represented by a peripheral vertex is referred to as a membrane compartment. We assume the membrane is one dimensional (we consider it to have zero thickness) and consider the concentration of polarity components in the membrane (of dimension quantity of substance per unit length) to have arbitrary units per µm (A_u/µm). In most models, the single central vertex of each cell is used to represent the cytoplasm of that cell and the cytoplasm is not further discretised. This is because diffusion of the inactive polarity components (A and B) in the cytoplasm is assumed to be relatively fast. Therefore, for simplicity, the concentrations of A and B are assumed to always be evenly distributed throughout the cytoplasm, removing the need for further discretisation of the cytoplasm and simulation of diffusion. In the simulation used to generate Fig. 4F,G, where effective diffusion rates in the cytoplasm are set to be the same as those in the membrane, diffusion in the cytoplasm is simulated. In these simulations, diffusion in the cytoplasm is treated in the same way as diffusion in the membrane, to ensure comparability. This is carried out by using each peripheral vertex to represent a region of the

cytoplasm underlying the membrane. In the following descriptions, the region of cytoplasm represented by a central or a peripheral vertex is referred to as a cytoplasmic compartment. In all simulations except those used to generate Fig. 4F,G, the concentration of polarity components in the cytoplasm is considered to have arbitrary units (A_u) per unit area ($A_u/\mu m^2$). In the simulations used to generate Fig. 4F,G, the cytoplasmic polarity components have units of $A_u/\mu m$.

In the case where cells have regular hexagonal geometries, each of the six edges of the hexagon is considered to have a length of 10 µm. Each of the six edges is represented by four peripheral vertices (black dots in Fig. S1); therefore, each cell contains 24 peripheral vertices. Each peripheral vertex has a length associated with it of 2.5 µm. The area of each cell is 260 μm^2 and the minimal diameter of the cell is 17.3 µm. In simulations with square cells, each of the four cell edges of the cell has a length of 13 µm and is represented with five peripheral vertices, each with a length of 2.6 µm. The area of the cell is 169 μm^2. In simulations with irregular cell geometries, the average dimensions are approximately the same as for regular cells, but the exact dimensions may vary between cells and the lengths associated with peripheral vertices may vary slightly within an individual cell. The dimensions of all cells remain the same throughout all simulations.

In the case where the cytoplasm is represented by the single central vertex of each cell, the area of the cytoplasm is considered to be equal to the geometrical area of the whole cell. In all simulations, the length of each membrane compartment is the length associated with the peripheral vertex it is represented by. In the simulations used to generate Fig. 4F,G, the length associated with each compartment of cytoplasm is the same as the length of the peripheral vertex used to represent it.

At the beginning of all simulations, the intracellular partitioning system is initialized with a default concentration of polarity components in each cytoplasmic compartment,

$$A(t = 0) = c_A \quad (1a),$$

$$B\ (t = 0) = c_B \quad (1b),$$

where *A(t=0)* and *B(t=0)* are the initial concentrations of A and B polarity components in cytoplasmic compartments and c_A and c_B are the default initial concentrations of A and B polarity components respectively.

In all simulations except those used to generate Figs 6, 11F,G, $c_A = c_B = 0.02\ A_u/\mu m^2$ in all cells. In the simulations used to generate Figs 6, 11F,G, in the column of cells on the left of the tissue (which has only A and A*) $c_B = 0\ A_u/\mu m^2$; in the column of cells on the right of the tissue (which has only B and B*) $c_A = 0\ A_u/\mu m^2$. In Fig. 10D, $c_A = 0\ A_u/\mu m^2$ in the column of cells on the right of the tissue. In Fig. 4F,G, $c_A = c_B = 0.2\ A_u/\mu m$.

Noise is added to the system during the initialization of the concentrations of A* and B*. In each of the membrane compartments, the concentration of A* and B* is set to a default concentration plus or minus a randomly generated value:

$$A^*(t=0) = d_A(1+\theta_A) \quad (2a),$$

$$B^*(t=0) = d_B(1+\theta_B) \quad (2b),$$

$$\theta_{A,B} \in [-\varepsilon, \varepsilon] \quad (2c).$$

Here *A**(*t=0*) and *B**(*t=0*) are the initial concentrations of polarity components in a given membrane compartment and d_A and d_B are the default initial concentrations of A* and B* membrane-bound polarity components, respectively. θ_A and θ_B are independently generated random numbers uniformly distributed between an upper and lower limit, ε. This method used to initialize the system introduces small differences between the total amounts of the A polarity component (A* + A) and the total amounts of the B polarity component (B* + B) in each cell. It also introduces variation between cells in the total amounts of polarity components per cell. In all simulations except those used to generate Figs 6, 11F,G, $d_A = d_B = 0.3$ $A_u/\mu m$ and ε = 0.25 for all cells. In Figs 6, 11F,G, in the column of cells on the left of the tissue, $d_B = 0$ $A_u/\mu m$; in the column of cells on the right of the tissue, $d_A = 0$ $A_u/\mu m$. In Fig. 10D, $d_A = 0$ $A_u/\mu m$ in the column of cells on the right of the tissue.

Following initialization of the system, reactions between the polarity components are simulated. All changes in concentration are solved numerically using an explicit Euler integration method. Reactions are first described for the case where the cytoplasm is represented by the single central vertex of each cell (this is the case in all simulations except those used for Fig. 4F,G). With intracellular partitioning, the concentrations of A* and B* in a given membrane compartment depend on five processes: (1) A and B bind to the membrane; (2) A* and B* unbind from the membrane; (3) membrane-bound polarity components promote the membrane-binding of their own polarity component through auto-activation (i.e. A* in a membrane compartment promotes the binding of A to that membrane compartment); (4) membrane-bound polarity components promote the unbinding of the opposite polarity component through mutual inhibition (i.e. A* in a membrane compartment promotes the unbinding of B* from that membrane compartment and vice-versa); (5) membrane-bound polarity components diffuse between the membrane compartments of the same cell. The equation describing the rate of change of A* concentration for a given membrane compartment is

$$\frac{\partial A^*}{\partial t} = (\rho + \eta A^*)A - (\mu + \alpha B^*)A^* + D_{A^*}\nabla^2 A^* \quad (3a),$$

where *A** and *B** are the concentrations of the polarity components in the membrane compartment with units of $A_u/\mu m$, and *A* is the concentration of the A polarity component in the cytoplasmic compartment of the same cell with units of $A_u/\mu m^2$. ρ is the membrane-binding rate of polarity components with units of μm/s, η describes the extent to which membrane-bound polarity components promote the binding of their own polarity component (auto-activation) and has units of $\mu m^2/A_u.s$, μ is the unbinding rate with units of /s, and α is the rate of cross-inhibition between membrane-bound polarity components with units of $\mu m/A_u.s$. D_{A^*} is the diffusion constant of A* in the membrane with units of $\mu m^2/s$.

The corresponding equation describing the rate of change of B* concentration for a given membrane compartment is:

$$\frac{\partial B^*}{\partial t} = (\rho + \eta B^*)B - (\mu + \alpha A^*)B^* + D_{B^*}\nabla^2 B^* \quad \text{(3b)},$$

where B^* and A^* are the concentrations of the polarity components in the membrane compartment and B is the concentration of the B polarity component in the cytoplasmic compartment of the same cell. ρ, η, μ and α are as described for Equation 3a (for simplicity it is assumed that both polarity components behave with the same dynamics). D_{B^*} is the diffusion constant of B* in the membrane with units of $\mu m^2/s$ (we assume $D_{A^*} = D_{B^*}$). As there is only one cytoplasmic compartment per cell, the concentrations of A and B available to each membrane compartment of a cell are the same. This captures the relatively high diffusion rates that are assumed for the inactive polarity components.

In simulations where the basic intracellular partitioning mechanism is modified by introduction of cell-cell coupling or interactions with tissue gradients, Equations 3a and 3b are modified. In order to describe these modifications to intracellular partitioning, it is useful to describe intracellular partitioning in terms of more general equations. Equations 3a and 3b can be described in terms of a general binding function, a general unbinding function and a diffusion term. In the case of intracellular partitioning, the binding and unbinding functions each have a single argument, and therefore the general functions are described as having a single argument below. However, in different model variants, the binding and unbinding functions can have A* or B*, or both, as arguments. The equations for intracellular partitioning in membrane compartments (Equations 3a and 3b) in general terms are

$$\frac{\partial A^*}{\partial t} = f_A(A^*)A - g_A(B^*)A^* + D_{A^*}\nabla^2 A^* \quad \text{(4a)},$$

where

$$f_A(A^*) = \rho + \eta A^* \quad \text{(4b)},$$

$$g_A(B^*) = \mu + \alpha B^* \quad \text{(4c)},$$

$$\frac{\partial B^*}{\partial t} = f_B(B^*)B - g_B(A^*)B^* + D_{B^*}\nabla^2 B^* \quad \text{(4d)},$$

where

$$f_B(B^*) = \rho + \eta B^* \quad \text{(4e)},$$

$$g_B(A^*) = \mu + \alpha A^* \quad \text{(4f)}.$$

Here, f_A (A^*) and f_B (B^*) are the general functions determining membrane-binding of A and B, respectively, and g_A (B^*) and g_B (A^*) are the general functions determining unbinding of A* and B*, respectively.

For simplicity, the polarity components are assumed to undergo conversion between cytoplasmic and membrane-bound forms without any change in the total amounts of A + A* or B + B* (there is no production or degradation of polarity components). Over a given time interval, the changes in the total amounts of A and B in a cytoplasmic compartment are the opposite of the sum of the changes in the total amounts of A* and B* in all the membrane compartments of a cell. The rate of change in the concentration of the A polarity component in the cytoplasmic compartment (c) of a cell is

$$\frac{\partial A}{\partial t} = \frac{-1}{R_c}\sum_{n\in N(c)} l_n\left(f_A(A_n^*)\,A - g_A(B_n^*)A_n^*\right) \qquad (5)$$

where A is the concentration of the A polarity component in the cytoplasmic compartment, c, and A_n^* is the concentration of the A* polarity component in the membrane compartment n, in the neighborhood of c ($N(c)$). R_c is the area of the cytoplasmic compartment and l_n is the length of the nth membrane compartment. f_A (A_n^*) is the general function determining binding of A and g_A (B_n^*) is the general function determining unbinding of A_n^*, for the membrane compartment n in the same cell as the cytoplasmic compartment. In the case of intracellular partitioning alone, f_A (A_n^*) is the same as described by Equation 4b and g_A (B_n^*) is the same as described by Equation 4c. The equation for the B polarity component is equivalent to that shown above for A.

In all simulations, the parameters values used for intracellular partitioning are: ρ = 0.02 μm /s, η = 0.2 $\mu m^2/A_u$.s, μ = 0.002 /s, α = 0.04 $\mu m/A_u$.s. $D_A = D_B$ = 0.1 μm^2/s. This value for the diffusion constant is the same as previously estimated for membrane-bound G-proteins (Postma et al., 2004; Postma and Van Haastert, 2001). In simulations with regular hexagons, R_c = 260 μm^2 and l_n = 2.5 μm. In simulations with irregular hexagonal geometries, the average values are R_c = 260 μm^2 and l_n = 2.5 μm but the exact values can vary between cells and between membrane compartments of the same cell. In simulations with square cells, R_c = 169 μm^2 and l_n = 2.6 μm.

Direct cell-cell coupling

In simulations involving direct cell-cell coupling (Fig. 4E-H, Fig. 6A,B, Fig. 8D, Fig. 9, Fig. 11A,D,F,H), A* in a membrane compartment of a given cell (cell 1) is assumed to interact with B* in the juxtaposed membrane compartment of an adjacent cell (cell 2) to form an intercellular A*-B* bridging complex. The intracellular partitioning mechanism described above is modified such that auto-activation and cross-inhibition depend on formation of this complex. The A*-B* bridging complex enhances A* and inhibits B* in the membrane compartment of cell 1 (which is at the A* side of the complex), while enhancing B* and inhibiting A*in the juxtaposed membrane compartment of cell 2 (which is at the B* side of the complex). Thus, in the case of direct cell-cell coupling, the binding and unbinding functions of the general equations (Equations 4a and 4d) have complex-dependent auto-activation and cross-inhibition terms. In the case of direct cell-cell coupling, the binding and unbinding functions take two arguments. For example, in addition to A*, the binding function for A* (f_A) takes B* in the juxtaposed membrane

compartment of the neighboring cell (which we refer to as B*') as an argument. The binding and unbinding functions for direct cell-cell coupling, which can be inserted into the general Equations 4a and 4d are

$$f_A(A^*, B^{*\prime}) = \rho + \omega A^* B^{*\prime} \quad (6a),$$

$$g_A(B^*, A^{*\prime}) = \mu + \upsilon B^* A^{*\prime} \quad (6b),$$

$$f_B(B^*, A^{*\prime}) = \rho + \omega B^* A^{*\prime} \quad (6c),$$

$$g_B(A^*, B^{*\prime}) = \mu + \upsilon A^* B^{*\prime} \quad (6d).$$

where *A** and *B** are the concentrations of polarity components in a given membrane compartment and *B*'* and *A*'*are the concentrations of polarity components in the juxtaposed membrane compartment of the neighboring cell. Thus, we assume that the concentrations of A*-B* and B*-A* complexes are proportional to *A*B*'* and *B*A*'* respectively. Such a mass-action term is a reasonable approximation if the concentration of complexed polarity components is small relative to the uncomplexed components. ω is the rate at which a polarity component complex promotes the membrane binding of the inwardly pointing polarity component type in the same membrane compartment (auto-activation) with units of $\mu m^3/A_u^2.s$. υ is the rate at which a polarity component complex promotes unbinding from the membrane of the polarity component type opposite to that which is inwardly pointing in the complex (cross-inhibition) with units of $\mu m^2/A_u^2.s$.

In all simulations involving direct cell-cell coupling, except the simulations used to generate Fig. 4F,G, the parameter values used are ω = 0.54 $\mu m^3/A_u^2.s$ and υ = 0.023 $\mu m^2/A_u^2.s$. The values of ρ and μ are the same as for intracellular partitioning alone (ρ = 0.02 µm/s, μ = 0.002 /s).

In the simulations used to generate Fig. 4F,G, in order to simulate diffusion in the cytoplasm, it is represented by peripheral vertices. The rates of change of active, membrane-bound polarity components in a given membrane compartment depend on the concentrations of inactive polarity components in the associated cytoplasmic compartment, which is represented by the same peripheral vertex as the given membrane compartment. The simulation of direct cell-cell coupling for membrane-bound polarity components is as described above (Equations 6a-6d along with Equations 4a and 4d). However, the general equation describing the rate of change of inactive polarity component A in a given cytoplasmic compartment (Equation 5) is changed to include a diffusion term:

$$\frac{\partial A}{\partial t} = -(f_A(A^*)A - g_A(B^*)A^*) + D_A \nabla^2 A \quad (7a),$$

where *A* is the concentration of the inactive polarity component A in a given cytoplasmic compartment and *A** and *B** are the concentrations of active polarity components in the membrane compartment represented by the same peripheral vertex. D_A is the diffusion constant for A in the cytoplasm, with units

of $\mu m^2/s$. Unlike Equation 5, these equations do not involve multiplication by the length of the membrane compartment and division by the area of the cytoplasmic compartment because in this case the cytoplasmic compartment has the same dimensions as the membrane compartment with which polarity components are being exchanged. The equation for B is equivalent to that shown for A.

The specific binding and unbinding functions, and the parameter values used, are as described above for direct cell-cell coupling (Equations 6a-d) except that here, ρ has units of /s with a value of 0.002 and ω has units of $\mu m^2/A_u^2.s$ with a value of 0.054. In all cells in Fig.4F, and in all cells except the central cell in Fig.4G, $D_{A^*} = D_{B^*} = D_A = D_B$=0.1 $\mu m^2/s$. In the central cell in Fig.4G, $D_{A^*} = D_{B^*}$ =0.1 $\mu m^2/s$ and $D_A = D_B$= 2.5 $\mu m^2/s$.

A model for direct cell-cell coupling is presented in which the A* - B* membrane-spanning complex inhibits A* at the B* end of the complex, while uncomplexed A* and B* undergo auto-activation and cross-inhibition (Fig.4A,D). In this model, the binding and unbinding and functions are

$$f_A(A^*) = \rho + \eta A^* \quad (8a),$$

$$g_A(B^*, A^{*\prime}) = \mu + \alpha B^* + \upsilon B^* A^{*\prime} \quad (8b),$$

$$f_B(B^*) = \rho + \eta B^* \quad (8c),$$

$$g_B(A^*) = \mu + \alpha A^* \quad (8d),$$

where A^* and B^* are the concentrations of polarity components in a given membrane compartment and $A^{*\prime}$ is the concentration of A* in the juxtaposed membrane compartment of the neighboring cell. v is the complex-dependent cross-inhibition rate with units of $\mu m^2/A_u^2.s$ (as for Equations 6b and 6d, the same parameter value was used), ρ, μ, η and α and the values used for these parameters are as described for intracellular partitioning (as for Equation 3a).

Tissue gradients

Simulations involving gradients of a signal, S (Figs 8, 9, 11C,H), are performed in two phases. In the first phase, a gradient in S is established in an extracellular space without simulation of intracellular partitioning or direct cell-cell coupling. In the second phase, the distribution of S is assumed to remain constant and intracellular partitioning or direct cell-cell coupling under the influence of S (or factor F, produced in response to S) is simulated.

The intracellular partitioning graph (Fig. S1) does not include a representation of the extracellular space. Therefore, the production, degradation and diffusion of S is simulated on a different graph that represents only the extracellular space (Fig. S2). This extracellular space graph contains multiple vertices

and connections between them. Each vertex of the extracellular space graph is positioned at a vertex of the cell and each edge of the extracellular space graph corresponds to a cell edge. We refer to each vertex of the extracellular space graph as an extracellular space compartment. In simulations where both the extracellular space graph and the intracellular partitioning graph are used, the peripheral vertices of the intracellular partitioning graph are positioned so that they map on to the extracellular space graph (four peripheral vertices of the intracellular partitioning graph are positioned along each edge of the extracellular space graph). In simulations using cells with regular hexagonal geometries, the distance between neighboring vertices in the extracellular space graph is 10 µm, which is equivalent to the length of hexagon edges in the intracellular partitioning graph. In simulations using cells with square geometries, the distance between vertices is 13 µm. In simulations with irregular cell geometries, the dimensions of the extracellular space graph may vary but on average are approximately the same as in simulations with regular cell geometries. The concentration of S is per unit length of the extracellular space compartment and has units of A_u/µm.

The equation governing the rates of change of S concentration in extracellular space compartments is

$$\frac{\partial S}{\partial t} = \rho_s - \mu_s S + D_s \nabla^2 S \qquad (9),$$

where ρ_s is the production rate of S (which is high in the file of cells acting as a source of S) with units of A_u/µm.s. μ_s is the degradation rate of S (which is high in the file of cells acting as a sink for S) with units of /s and D_s is the diffusion rate of S within the extracellular space with units of μm^2/s.

In all simulations involving cellular gradients, $\rho_s = 10^{-5}$ A_u/µm.s and $\mu_s = 10^{-4}$ /s everywhere except in the column of cells at the left tissue boundary, which acts as a source of S, where $\rho_s = 5 \times 10^{-4}$ A_u/µm.s and in the column of cells at the right tissue boundary, which acts as a sink of S, where $\mu_s = 7.5 \times 10^{-3}$ /s. D_s = 5 μm^2/s. In the simulation used to generate Fig. 8C where a mutant patch is introduced that degrades S at a higher rate than the background degradation rate in surrounding cells, in all cells except those in the left/rightmost columns of cells, which act as a source/sink for S, $\rho_s = 10^{-4}$ A_u/µm.s and $\mu_s = 10^{-4}$ /s. In the leftmost column of cells, which acts as a source of S, $\rho_s = 5 \times 10^{-4}$ A_u/µm.s and in the rightmost column of cells, which acts as a sink of S, $\mu_s = 4 \times 10^{-3}$ /s. In the mutant patch, μ_s = 0.014 /s.

After the distribution of S becomes stable, the concentrations of S in the extracellular space graph are used to influence components in the intracellular partitioning graph. It is assumed that extracellular S triggers receptors in cell membranes, and that the activity of these receptors influences the intracellular partitioning system. The extracellular space graph is more coarsely discretised than the intracellular partitioning graph [there are fewer vertices surrounding a cell in the extracellular space graph (Fig. S2) than peripheral vertices surrounding a cell in the intracellular partitioning graph (Fig. S1)]. Therefore, before using concentrations of S from the extracellular space graph to influence components in the intracellular partitioning graph, the concentrations of S are linearly interpolated between vertices in the extracellular space graph. These interpolated concentrations, S_i, are then used to set S_p in membrane compartments represented by peripheral vertices in the intracellular partitioning graph. At the boundary between two adjacent cells, the membrane compartments of both cells are given the same

concentration of S_i (i.e. there no gradients in S or S_i across the thickness of the intercellular space). After transferring the concentrations of S to the intracellular partitioning graph, noise is added to the concentration of S in the membrane compartments to simulate stochasticity involved in the establishment and perception of the S gradient and to allow robustness of mechanisms to be evaluated:

$$S_p = S_i \pm (\theta_s * \sqrt{S_i}) \quad (10a),$$

$$\theta_s \in [-\varepsilon_s, \varepsilon_s] \quad (10b),$$

where S_p is the concentration of S perceived in a given membrane compartment with units of $A_u/\mu m$, S_i, is the interpolated concentration of S and θ_s is a random number uniformly distributed between an upper and lower limit, ε_s. In all simulations, $\varepsilon_s = 0.25$. Noise is added to the concentration of S_i in proportion to $\sqrt{S_i}$.

In the second phase of simulations involving cellular gradients in S_p influencing the intracellular partitioning system (Figs 8, 11C), the concentrations of S_p in membrane compartments are assumed to remain constant and S_p is used to promote the membrane binding of the A* polarity component. In the case where S_p promotes the activation of A, the binding and unbinding functions of the basic intracellular partitioning system (Equations 4b and 4c) are modified so that the functions for A* in a given membrane compartment are

$$f_A(A^*, S_p) = \rho + \gamma_s S_p + \eta A^* \quad (11a),$$

$$g_A(B^*) = \mu + \alpha B^* \quad (11b),$$

Where γ_s is a constant describing the strength of promotion of A binding by S_p with units of $\mu m^2/A_u.s$. The functions for B* are the same as for intracellular partitioning alone (Equations 4e and 4f).

In all simulations where cellular gradients influence intracellular partitioning, except that used for Fig. 8D (Figs 8A-C, 11C), $\gamma_s = 0.25\ \mu m^2/A_u.s$.

In the simulation used to generate Fig. 8D, cellular gradients operate in combination with the direct cell-cell coupling system and the direct cell-cell coupling equations (Equations 6a and 6b) are modified as follows:

$$f_A(A^*, B^{*\prime}, S_p) = \rho + \gamma_s S_p + \omega A^* B^{*\prime} \quad (12a),$$

$$g_A(B^*, A^{*\prime}) = \mu + \upsilon B^* A^{*\prime} \quad (12b),$$

In this simulation, $\gamma_s = 0.5\ \mu m^2/A_u.s$

In simulations where the intercellular gradient in S is used to influence polarity coordination (Figs 9A,B, 11H), S_p promotes production of a factor, F, within each cell. In these simulations, after the calculation of concentrations of S_p in the membrane compartments of the intracellular partitioning graph, including the addition of noise, the concentration of F in cytoplasmic compartments is calculated. The concentration of F in cytoplasmic compartments is assumed to be proportional to the total concentration of S perceived by membrane compartments and is calculated as

$$F = \lambda \frac{1}{R_c} \sum_{n \in N(c)} l_n S_n \quad (13),$$

where F is the concentration of F in a given cytoplasmic compartment with units of $A_u/\mu m^2$, λ is a dimensionless constant describing the relationship between the concentration of S_p in membrane compartments and the concentration of F in the cell and R_c is the area of the cytoplasmic compartment. S_n is the concentration of S (S_p) in the membrane compartment n in the neighborhood of the cytoplasmic compartment c ($N(c)$), with units of $A_u/\mu m$, l_n is the length of the membrane compartment n, with units of μm. In all simulations, λ =0.1.

Once the concentration of F in cytoplasmic compartments has been calculated, F is used to influence the levels of A in cytoplasmic compartments (and therefore the total level of A + A* in a cell) during the initialization of the intracellular partitioning system:

$$A(t=0) = c_A(1 + \Omega F) \quad (14a),$$

$$B(t=0) = c_B \quad (14b),$$

where $A(t=0)$ and $B(t=0)$ are the initial concentrations of polarity components in a given cytoplasmic compartment, F is the concentration of F in the cytoplasmic compartment, c_A and c_B are the default concentrations of A and B, respectively, in the cytoplasm, and Ω is a constant with units of $\mu m^2/A_u$, describing the strength of promotion of the levels of A by F. The initialization of A* and B* concentrations in membrane compartments occurs as described for intracellular partitioning in the previous section and is not influenced by F. In all simulations, Ω =70 $\mu m^2/A_u$.

Following the F-influenced initialization of the system, the interactions between the polarity components are simulated in the same way as for direct cell-cell coupling.

Indirect cell-cell coupling

For the implementation of indirect cell-cell coupling, the intracellular partitioning graph is modified to include another set of vertices in addition to central and peripheral vertices. We refer to this modified graph as the cell wall graph (Fig. S3). The additional set of vertices is arranged to form a one dimensional network surrounding the cells. Each of these vertices represents a region of the cell wall (extracellular space) and the region of cell wall represented by one vertex is referred to as a cell wall compartment. Each cell wall compartment is connected to its immediately neighboring cell wall compartments and to the neighboring membrane compartments that belong to the two cells separated by the wall. Therefore,

in indirect cell-cell coupling models, membrane compartments of adjacent cells are always separated by a single cell wall compartment. This means concentration gradients cannot occur across the thickness of the cell wall.

In simulations involving indirect cell-cell coupling (Figs 5, 6C, 10, 11B,E,G,I), a mediator molecule, M, coordinates polarities by interacting with the intracellular partitioning system. In all simulations of indirect cell-cell coupling, the cytoplasm is represented by the single central vertex of each cell. M is present in the cytoplasm (intracellular M) and in wall compartments (extracellular M) but is not present in membrane compartments. M can diffuse between neighboring cell wall compartments in the extracellular space. The diffusion of M within the cytoplasm is assumed to be relatively fast and therefore, for simplicity, M is assumed to always be evenly distributed in the cytoplasm. Simulations using the alternative assumption that M is not uniformly distributed throughout the cytoplasm were performed and gave similar results to those presented. The diffusion of M in the extracellular space is assumed to be 100-fold faster than diffusion of polarity components in the membrane. This assumption of a two order of magnitude difference is based on experimental estimates of the diffusion constant of small auxin-like molecules in the plant cell wall being between 2.5 and 32 $\mu m^2/s$ (Kramer et al., 2007), compared with 0.1 $\mu m^2/s$ for membrane-bound proteins (Postma and Van Haastert, 2001). The units of M concentration in the cytoplasm and in the wall are $A_u/\mu m^2$. During initialization of the simulation, M concentrations in cell wall compartments are set to zero and M concentrations in the cytoplasm are set to 0.8 $A_u/\mu m^2$. The wall is assumed to have uniform thickness (1 µm).

M is produced and degraded in the cytoplasm. In simulations with irregular cell geometries, production of M occurs in proportion to the area of the cytoplasm. Using an alternative assumption, that each cell has the same total production of M, rather than producing M in proportion to the area of the cytoplasm, gives qualitatively similar results. In addition to diffusing through the extracellular space, M undergoes permeation between the cell wall and the cytoplasm. The permeability rate of M into the cell (into the cytoplasmic compartment from a wall compartment) is assumed to be 15-fold higher than the permeability rate of M out of the cell (into a wall compartment from a cytoplasmic compartment). M is transported out of cytoplasmic compartments in an A*-dependent manner (A* in each membrane compartment promotes export of M from the cytoplasm to the adjacent wall compartment). The rate of change in M concentration in a given cytoplasmic compartment for cells with regular geometries is calculated as

$$\frac{\partial M}{\partial t} = \rho_m - \mu_m M + \frac{1}{R_c} l_w \sum_{n \in N(c)} (\nu_{\text{in}} M_w - \nu_{\text{out}} M - \psi A_n^* M) \qquad (15),$$

where M is the concentration of M in the cytoplasmic compartment, M_w is the concentration of M in the wall compartment neighboring the membrane compartment n in the neighborhood of the cell c ($N(c)$), ρ_m is the production rate of M with units of $A_u/\mu m^2.s$, R_c is the area of the cytoplasmic compartment, and μ_m is the degradation rate of M with units of /s. A_n^* is the concentration of A* in the *nth* membrane compartment of the cell. v_{in} is the background permeation rate of M into the cytoplasm from the wall with units of µm/s and v_{out} is the background permeation rate of M into the wall from the cytoplasm

with units of μm/s. ψ is the rate of A*-dependent active efflux of M from the cytoplasm into the wall with units of $\mu m^2/A_u.s$. The permeation and active efflux terms ($v_{in} M_w - v_{out} M - \Psi A_n^* M$) describe the flux of mediator between the cytoplasm and the wall compartment adjacent to the *nth* membrane compartment and have units of number of molecules per unit time per unit length of contact between the cell wall compartment and the cell ($A_u/\mu m.s$). In order to convert the flux terms into a concentration of M in the cytoplasm, flux terms are multiplied by the length of the cell wall compartment into/out of which flux is occurring (l_w) (this gives the total number of molecules per unit time), and divided by the area of the cytoplasm (R_c) (this converts the total number of molecules to a concentration for the cytoplasmic compartment).

The corresponding equation for cell wall compartments is

$$\frac{\partial M_w}{\partial t} = -\frac{1}{R_w} l_w \sum_{n \in N(w)} (\nu_{\text{in}} M_w - \nu_{\text{out}} M_c - \psi_o A_n^* M_c) + D_m \nabla^2 M_w \qquad (16),$$

where R_w is the area of the wall compartment, l_w is the length of the wall compartment, M_w is the concentration of M in the wall compartment, A_n^* is the concentration of A* in the membrane compartment n in the neighborhood of the given wall compartment w ($N(w)$) and M_c is the concentration of M in the cytoplasm of the same cell as the membrane compartment n. D_m is the diffusion constant for M within the cell wall with units of $\mu m^2/s$ (this constant relates to lateral diffusion between wall compartments as it is assumed that the concentration of M is uniform across the thickness of the wall).

In all simulations, D_m =10 $\mu m^2/s$, v_{in} =0.75 μm/s, v_{out} =0.05 μm/s, ψ = 7.5 $\mu m^2/A_u.s$. In all cells and in all simulations, except in the left- and rightmost files of cells in the simulations used to generate Figs 10A-D and 11I, ρ_m =1.3 × 10^{-4} $A_u/\mu m^2.s$ and μ_m=0.02 /s. In the simulation used to generate Figs 10A,B, 11I, in the leftmost column of cells which acts as a source of M, ρ_m =10^{-3} $A_u/\mu m^2.s$ and in the rightmost column of cells, which acts as a sink of M, μ_m=0.3 /s. In the simulations used to generate Fig. 10C,D, in the leftmost column of cells, which acts as a source of M, ρ_m =3×10^{-4} $A_u/\mu m^2.s$ and in the rightmost column of cells, which acts as a sink of M, μ_m=0.05 /s.

Extracellular M within each cell wall compartment interacts with the intracellular partitioning system by promoting the unbinding of A* in the adjacent membrane compartments. The influence of extracellular M on A* is described by the following modification to the general unbinding function for A*in a given membrane compartment:

$$g_A(B^*, M_w) = \mu + \alpha B^* + \gamma_m M_w \qquad (17),$$

where B^* is the concentration of the B* polarity component in the given membrane compartment, M_w is the concentration of M in the adjacent wall compartment and γ_m is the strength of M-promoted conversion from A* to A with units of $\mu m^2/A_u.s$. The binding function for A*, as well as the binding and

unbinding functions for B*, remain the same as for the basic intracellular partitioning mechanism (Equations 4b, 4e, 4f, respectively). In all simulations involving indirect cell-cell coupling, $\gamma_m = 0.3$ $\mu m^2/A_u.s$.

Table S1. Parameter values used for simulations

Symbol	Description	Unit	Value	Range tested and found functional
Δt	Numerical time step	s (seconds)	0.01	
R_c	Area of cytoplasmic compartment	μm^2	260*/169**	
R_w	Area of cell wall compartment	μm^2	2.5*/2.6**	
l_e	Length of extracellular space compartment	µm	15 /26**	
l_n	Length of membrane compartments	µm	2.5*/2.6**	
l_w	Length of wall compartments	µm	2.5*/2.6**	
c_A, c_B	Default initial concentrations of A and B polarity components respectively	A_u (arbitrary units)/ μm^2	0.02‡,#	
d_A, d_B	Default initial concentrations of A* and B* polarity components respectively	A_u/µm	0.3‡	
ε	Limit for noise addition during initialization of A* and B* concentrations	Dimensionless	0.25	0.05-1.25
D_{A*}, D_{B*}	Diffusion coefficients of membrane-bound polarity components	μm^2/s	0.1	0.02-0.3
ρ	Membrane-bound polarity component default binding rate	µm/s	0.02#	0.004-0.06
μ	Membrane-bound polarity component default unbinding rate	/s	0.002	0.0004-0.006
η	Membrane-bound polarity component auto-activation rate	$\mu m^2/A_u$.s	0.2	0.1-1.0

α	Membrane-bound polarity component cross-inhibition rate	$\mu m/A_u.s$	0.04	0.02-0.08
ω	Complex-dependent auto-activation rate	$\mu m^3/A_u^2.s$	0.54#	0.27-2.7
ν	Complex-dependent cross-inhibition rate	$\mu m^2/A_u^2.s$	0.023	0.0046-1.15
ρ_s	Production rate of S	$A_u/\mu m.s$	$10^{-5‡}$	
μ_s	Degradation rate of S	/s	$10^{-4‡}$	
D_s	Extracellular S diffusion constant	$\mu m^2/s$	5	
γ_s	S-dependent promotion of A to A* conversion	$\mu m^2/A_u.s$	0.25#	
ε_s	Limit for noise addition to get $[S_p]$	Dimensionless	0.25	
λ	Promotion of F by S_p	Dimensionless	0.1	
Ω	Promotion of [A] by F during initialization	$\mu m^2/A_u$	70	
ρ_m	Production rate of M	$A_u/\mu m^2.s$	$1.3\times10^{-4‡}$	0.26- 6.5
μ_m	Degradation rate of M	/s	0.02‡	0.004-0.1
ν_{in}	Influx M permeability	μm/s	0.75	0.15-3.75
ν_{out}	Background M efflux permeability	μm/s	0.05	0.01-0.25
ψ	A*-dependent M permeability	$\mu m^2/A_u.s$	7.5	1.5-37.5
γ_m	M-dependent promotion of A* to A conversion	$\mu m^2/A_u.s$	0.3	0.06-1.5
D_M	M diffusion constant in the cell wall	$\mu m^2/s$	10	2-50

*In simulations with regular hexagonal cell geometries. In simulations with irregular hexagonal cell geometries, the exact value may vary from this average value.

**In simulations with square cell geometries.

‡See text for details of cases where this may differ in organizer regions at tissue boundaries.

See text for details of simulations where this value may differ from the default value given.

To test the functional ranges of parameter values, the values of parameters involved in intracellular partitioning and cell-cell coupling were individually increased or decreased by a factor of 5 and the effects on the generation of cell polarities and on the coordination of polarities in a 1D file of cells were assessed. For most parameters tested (ε, D_M, v_{in}, v_{out}, γ_m, ψ, ρ_m, μ_m, v) a fivefold increase or decrease in the value used does not disrupt polarity generation or coordination and the values of all parameters tested can be at least halved or doubled while preserving the general model behaviors.

FIGURES

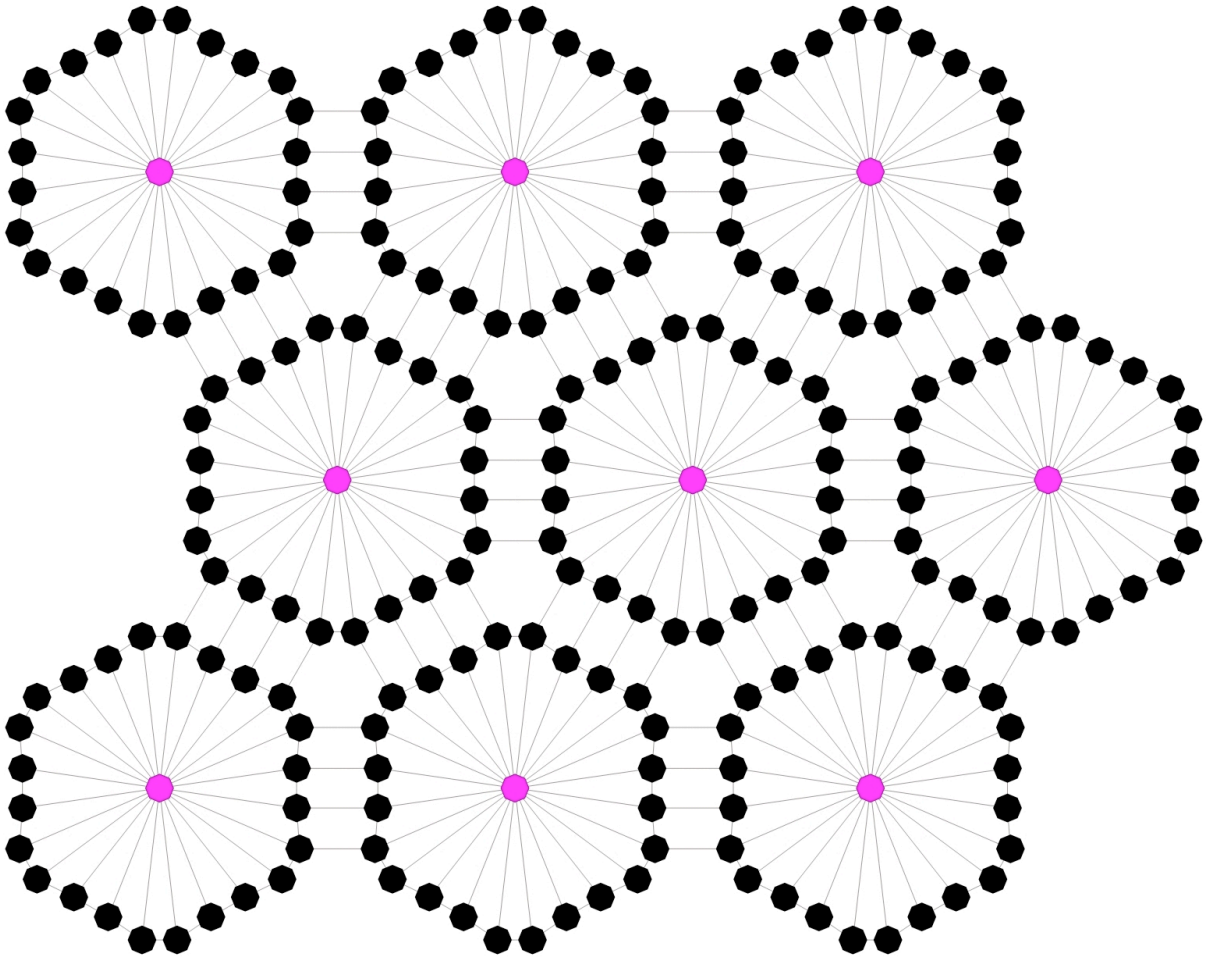

Fig. S1. The intracellular partitioning graph. Cells are represented by a single central vertex (magenta dots) surrounded by multiple peripheral vertices (black dots). The grey lines indicate the connections between vertices. Each central vertex is connected to all its surrounding peripheral vertices. Each peripheral vertex is connected to the central vertex of the same cell, its neighboring peripheral vertices in the same cell and the juxtaposed peripheral vertex of the adjacent cell.

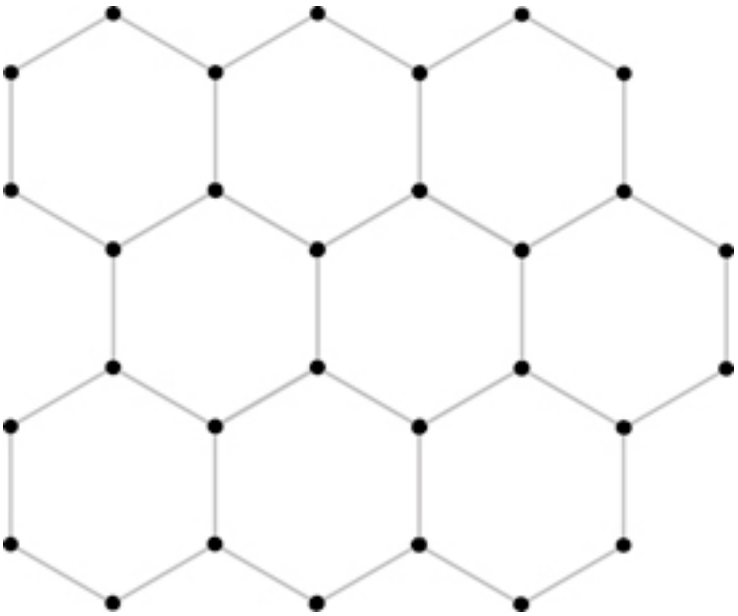

Fig. S2. The extracellular space graph. The extracellular space graph contains multiple vertices (black dots), each representing a compartment of extracellular space. Each vertex is connected to immediately neighboring vertices (gray lines).

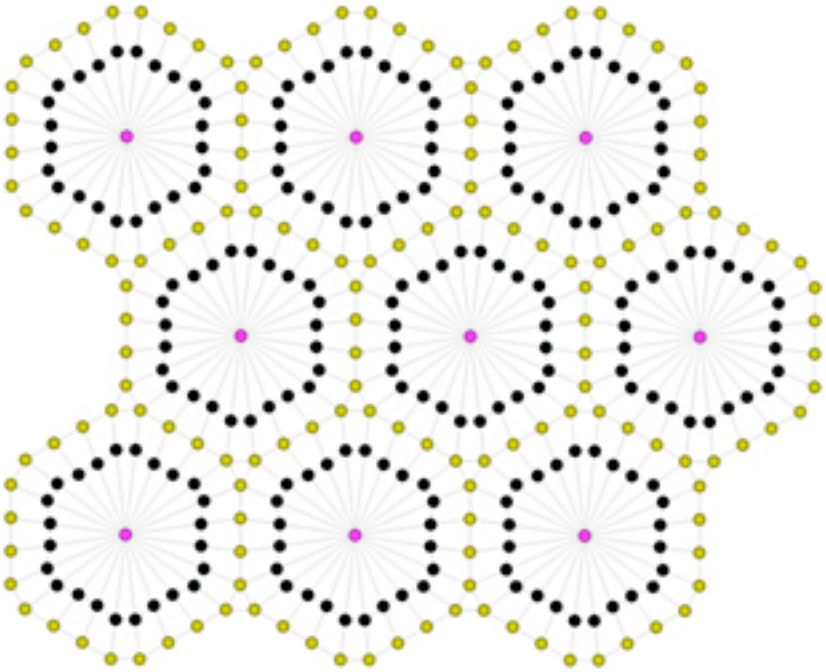

Fig. S3. The cell wall graph. As for the intracellular partitioning graph, cells are represented by a single central vertex (magenta) surrounded by multiple peripheral vertices (dark gray) that represent membrane compartments. In the cell wall graph, additional vertices surround cells and represent cell wall compartments (yellow). Using this representation, cell wall compartments separate the membrane compartments of adjacent cells. Cell wall compartments are connected to adjacent cell wall compartments and to the membrane compartments of adjacent cells that are separated by the cell wall. The gray lines indicate the connections between vertices and the compartments they represent.